

## RESEARCH ARTICLE

# Optimization and control of synchrotron emission in ultraintense laser–solid interactions using machine learning

J. Goodman<sup>1</sup>, M. King<sup>1,2</sup>, E. J. Dolier<sup>1</sup>, R. Wilson<sup>1</sup>, R. J. Gray<sup>1</sup>, and P. McKenna<sup>1,2</sup><sup>1</sup>SUPA Department of Physics, University of Strathclyde, Glasgow, UK<sup>2</sup>The Cockcroft Institute, Sci-Tech Daresbury, Warrington, UK

(Received 10 December 2022; revised 25 January 2023; accepted 6 February 2023)

**Abstract**

The optimum parameters for the generation of synchrotron radiation in ultraintense laser pulse interactions with planar foils are investigated with the application of Bayesian optimization, via Gaussian process regression, to 2D particle-in-cell simulations. Individual properties of the synchrotron emission, such as the yield, are maximized, and simultaneous mitigation of bremsstrahlung emission is achieved with multi-variate objective functions. The angle-of-incidence of the laser pulse onto the target is shown to strongly influence the synchrotron yield and angular profile, with oblique incidence producing the optimal results. This is further explored in 3D simulations, in which additional control of the spatial profile of synchrotron emission is demonstrated by varying the polarization of the laser light. The results demonstrate the utility of applying a machine learning-based optimization approach and provide new insights into the physics of radiation generation in laser–foil interactions, which will inform the design of experiments in the quantum electrodynamics (QED)-plasma regime.

**Keywords:** Bayesian optimization; gamma rays; laser–solid interactions; machine learning; radiation reaction**1. Introduction**

Irradiation of a solid target with a relativistically intense laser pulse typically produces a large number of photons with energies extending to the multi-MeV range, due to bremsstrahlung radiation from laser-accelerated electrons propagating through the target<sup>[1–3]</sup> and X-ray line emission from excited atomic states<sup>[4]</sup>. These bright sources of X-rays and gamma rays have potential applications including radiography<sup>[5–8]</sup>, initiating photonuclear reactions<sup>[1,9]</sup> and producing beams of positrons through the Bethe–Heitler process<sup>[10–14]</sup>. New multi-PW laser systems offer increased achievable peak laser intensities of approximately  $10^{23}$  W cm<sup>-2</sup><sup>[15]</sup>; with such intense laser light, higher energy photons will be produced than previously possible in these interactions, and the dominant mechanism for high-energy photon generation is expected to become synchrotron emission (nonlinear Compton scattering) from ultrarelativistic plasma electrons.

*1.1. Gamma ray generation*

The energy electrons can gain in a high-intensity laser field scaling with the parameter  $a_0 = eE_L/m_e c\omega_L \gg 1$ , where  $e$  is the elementary charge,  $E_L$  is the magnitude of the laser electric field,  $m_e$  is the electron rest mass,  $c$  is the speed of light in vacuum and  $\omega_L$  is the laser angular frequency. In moving to higher intensity laser pulses, electrons may become increasingly relativistic and generate more synchrotron radiation due to the increase in the field strength in their rest frame. This is expressed by the electron quantum parameter:

$$\chi_e = \frac{\gamma_e}{E_S} \sqrt{(\mathbf{E}_\perp + \mathbf{v}_e \times \mathbf{B})^2 + E_\parallel^2 / \gamma_e^2},$$

where  $\gamma_e$  is the electron Lorentz factor,  $\mathbf{v}_e$  is the electron velocity,  $\mathbf{E}_\perp$  is the electric field perpendicular to the electron motion,  $\mathbf{B}$  is the magnetic field,  $E_\parallel$  is the magnitude of the electric field parallel to the electron motion and  $E_S = 1.32 \times 10^{18}$  V m<sup>-1</sup> is the Schwinger field for which electron–positron pairs are produced from vacuum<sup>[16–18]</sup>. Here,  $\chi_e$  is dominated by the perpendicular fields for

Correspondence to: P. McKenna, SUPA Department of Physics, University of Strathclyde, Glasgow G4 0NG, UK. Email: paul.mckenna@strath.ac.uk

relativistic electrons, and is maximized for electrons counter-propagating with a laser pulse. For  $\chi_e \gtrsim 0.1$ , the electric field in the rest frame of the electron approaches the Schwinger field and a large fraction of the incident laser pulse energy may be converted into synchrotron gamma rays; the radiation reaction force on the emitting electrons becomes important and the high-energy photons in the laser field may produce electron–positron pairs through the multi-photon Breit–Wheeler process<sup>[19]</sup>. These strong-field quantum electrodynamics (QED) effects are expected to be a common feature of laser–plasma interactions for laser intensities  $I_L > 10^{23} \text{ W cm}^{-2}$ <sup>[20,21]</sup>.

All-optical demonstrations of radiation reaction with much lower laser intensities have been performed<sup>[22,23]</sup> in which a laser wakefield accelerated electron beam was collided with a laser pulse. Although higher laser intensities are required for the synchrotron radiation to become measurable in laser–solid interactions, theoretical and numerical studies indicate the generation of a high-power gamma ray flash with of the order of 10% conversion efficiency from the laser energy possible<sup>[24–29]</sup>. A large number of different interaction geometries and schemes have been proposed to enhance the gamma ray generation and associated pair production<sup>[29–54]</sup>. However, thus far experimental demonstration of a gamma ray source from a laser–solid interaction in which synchrotron radiation is dominant as compared with other generated sources, such as bremsstrahlung, has not occurred. This is key not only for the development of a new source of gamma radiation but also for experimental investigations of the underlying physics. Numerical modelling and theory show that bremsstrahlung emission is reduced by using a lower atomic number,  $Z$ , target material (given the emitted power scaling with  $Z^2$ )<sup>[14,55–58]</sup>. In addition, the use of thinner targets strongly reduces bremsstrahlung production<sup>[56,57,59]</sup>, including ultrathin (nanometre-scale) solid foils<sup>[59]</sup>.

### 1.2. Transparency

When an ultrathin foil is irradiated by a high-power laser pulse, the combined expansion of the target and heating of the electrons to relativistic velocities can reduce the plasma frequency ( $\omega_{pe} = \sqrt{n_e e^2 / \epsilon_0 \gamma_e m_e}$ ) to less than the laser frequency, and enable laser light propagation through the target plasma in the process known as relativistic self-induced transparency (RSIT)<sup>[60,61]</sup>. This is equivalent to the electron density,  $n_e$ , falling below the relativistic critical density ( $\gamma_e n_c = \gamma_e \epsilon_0 m_e \omega_L^2 / e^2$ ). The synchrotron emission can be particularly efficient in relativistically transparent targets, where much of the radiation is emitted by electrons that counter-propagate into the laser pulse, producing an angularly wide beam in the backward (with respect to the laser propagation) direction<sup>[24,26,59]</sup>, in a process termed re-injected electron synchrotron emission (RESE)<sup>[24]</sup>. Solid

targets also produce forward emitted synchrotron radiation from the reflected light interacting with electrons in the skin depth and oblique lobes either side of the laser propagation direction that are usually symmetric<sup>[26,57,59,62]</sup>. Although the conversion efficiency to synchrotron radiation is often lower for opaque targets compared with the maximum possible for those that experience RSIT, the introduction of a long pre-plasma density scale length on the target front surface can provide a large volume of transparent plasma to interact directly with the laser field and strongly increase the conversion efficiency<sup>[25,26,39,48]</sup>.

### 1.3. Optimization

There are many other parameters that can influence the generation of synchrotron radiation in these interactions, and finding the optimum conditions over a parameter search space with a large number of dimensions would be extremely costly and time consuming to achieve manually. In recent years, it has become possible to apply machine learning-based techniques as an efficient method of searching this multi-dimensional parameter space to find input conditions for the desired source parameters. Bayesian optimization<sup>[63,64]</sup> is one such technique that is useful when the objective function chosen to be optimized, such as the yield of gamma rays, is susceptible to noise and is costly to evaluate. This approach has already been demonstrated to improve electron and X-ray beams from wakefield accelerators<sup>[65,66]</sup> and laser-driven proton acceleration in simulations<sup>[67]</sup>. Other machine learning techniques that have been applied in the study of laser–plasma accelerators include neural networks<sup>[68,69]</sup> and evolutionary algorithms<sup>[70–73]</sup>.

### 1.4. Multiple objectives

The beam of high-energy particles or photons generated in these interactions is defined by many properties, such as the conversion efficiency, energy spectrum and divergence. For some applications, it is necessary to achieve several beam properties within a specific range and thus tune a number of the beam properties simultaneously. Often in such a scenario, these properties are individually optimized in different regions of the search space. Multi-objective optimization<sup>[74–77]</sup> involves finding a finite set of solutions that are located on the optimum edges of the objective space, known as the Pareto front, where one of the objectives cannot be improved without a trade-off in another. However, if only a single solution is desired, such as in the case of an automated laser-driven particle or radiation source guided by machine learning, it is not necessary to find a large set of solutions to choose between, and the problem can be reduced to the optimization of a single

objective function; although, this presents the challenge of combining the multiple objectives into a single composite function that is optimized at the most desirable location on the unknown Pareto front. Experimental optimization of laser–plasma accelerated electrons has been demonstrated with such a function incorporating multiple electron beam properties<sup>[65]</sup> and, in a simulation-based study<sup>[77]</sup>, different functions based on the same physical properties are demonstrated to optimize at different locations on the Pareto front found using multi-objective optimization.

In this paper, a numerical investigation, facilitated by the application of machine learning-based optimization, of the production of high-energy photons in the interaction of an ultraintense laser pulse with a thin solid foil is reported. In a number of 2D parameter space scans, using the BISHOP code<sup>[67]</sup>, the target foil thickness, the angle-of-incidence of the laser pulse and the laser pulse duration, focal spot size, defocus and peak intensity are varied to show the effect on the photon emission for p-polarized laser light (Section 3). For constant laser pulse energy, the conversion efficiency to synchrotron radiation is highest for parameters that maximize the peak laser intensity incident on the target surface, and oblique incidence provides a 60% increase in the conversion efficiency for the conditions tested. The synchrotron emission is also shown in 3D simulations to be highly susceptible to small changes in the focus position for a near-wavelength sized focal spot (required to maximize the emission) as a result of the micrometre-scale Rayleigh lengths for such focal spot sizes. A Gaussian process (GP) regression algorithm is then applied to control the input parameters for a series of simulations to optimize various physical properties of this source of high-energy photons individually. Multi-variate objective functions containing several different physical properties are then optimized, in which the bremsstrahlung emission is minimized whilst maximizing parameters of the synchrotron emission (Sections 4 and 5). The discovery of the angle-of-incidence as a critical input parameter in maximizing the directional emission of synchrotron radiation leads to further investigation and discussion of its influence on the interaction (Section 6), and motivates 3D simulations for different laser light polarization states to demonstrate control of the spatial profile of synchrotron emission (Section 7).

## 2. Methodology

The fully relativistic particle-in-cell (PIC) code EPOCH<sup>[78]</sup> was used in two and three dimensions to model the gamma ray generation in the interaction. Output data were generated individually for synchrotron and bremsstrahlung photons above 100 keV. The techniques used for calculating synchrotron emission in the EPOCH code are described in Ref. [79], and those used for calculating bremsstrahlung emission are described in Refs. [56,80]. For the 2D

simulations, the spatial grid had dimensions of  $30\ \mu\text{m} \times 20\ \mu\text{m}$  ( $x \times y$ ) and cell size  $8\ \text{nm} \times 12\ \text{nm}$ , with free-space boundaries. To simulate an experimentally practical low Z target material, solid density plastic (CH) was chosen and modelled as a uniform, fully ionized plasma with electron density  $n_e = 3.5 \times 10^{29}\ \text{m}^{-3}$ , neutralized by an equal ratio of  $\text{C}^{6+}$  and  $\text{H}^+$  ions. The initial electron and ion temperatures were 3 keV and 100 eV, respectively, with 50 electron macroparticles per cell and 10 ion macroparticles per cell per species. The target parameters were the thickness,  $l$ , and the angle between the normal to the target surface and the  $x$ -axis,  $\theta_i$ . The laser pulse was incident upon the target from the minimum  $x$  boundary, and had wavelength  $\lambda_L = 800\ \text{nm}$  and a Gaussian temporal-intensity profile with full width at half maximum (FWHM)  $\tau_L$ . The laser pulse was focused at  $x = x_f$ , where  $x = 0$  corresponds to the target irradiated (front) surface (the laser pulse focuses behind the target surface for  $x_f > 0$  and in front of the target for  $x_f < 0$ ) and  $x_f$  is the defocus parameter. At focus, the laser pulse has a Gaussian spatial-intensity profile with diameter  $\phi_L$  (FWHM). The values of  $l$ ,  $\theta_i$ ,  $\tau_L$ ,  $x_f$  and  $\phi_L$  used are stated in each section.

The 3D simulations used a spatial grid with dimensions  $20\ \mu\text{m} \times 15\ \mu\text{m} \times 15\ \mu\text{m}$  ( $x \times y \times z$ ) and cell size  $10\ \text{nm} \times 30\ \text{nm} \times 30\ \text{nm}$ . The target density was reduced to an electron density of  $n_e = 1.74 \times 10^{29}\ \text{m}^{-3}$  due to the increased cell size, whilst maintaining the areal density of the quoted target thicknesses in Section 7 by modelling an increased thickness. There were 12 electron macroparticles per cell and 6 ion macroparticles per cell per species.

The BISHOP code was used in conjunction with EPOCH to automate the 2D PIC simulations in 2D grid scans of various parameters, and for the Bayesian optimization of various objectives using a GP regression algorithm<sup>[81]</sup>, in the same manner as the code used in Ref. [67]. For all optimization scans, 30 initial simulations are performed with randomly generated input parameters (10 more than used previously<sup>[67]</sup> due to one more input parameter), the objective function is evaluated from the simulation data and the algorithm produces a probability distribution of all potential functions that could fit the results to create a model of the objective function. An acquisition function calculated from the model then determines the next set of input parameters to simulate. Acquisition functions corresponding to the upper confidence bound, expected improvement and probability of improvement methods are calculated and one of these is chosen at each iteration in a process known as hedging, which outperforms the use of individual acquisition functions in identifying the optimum in the minimum number of iterations<sup>[82]</sup>. With each iteration the model is updated and the acquisition function guides the parameters towards the optimum of the objective function. Up to 200 simulations were run for each objective function used to identify their respective optimum. The optimization parameters

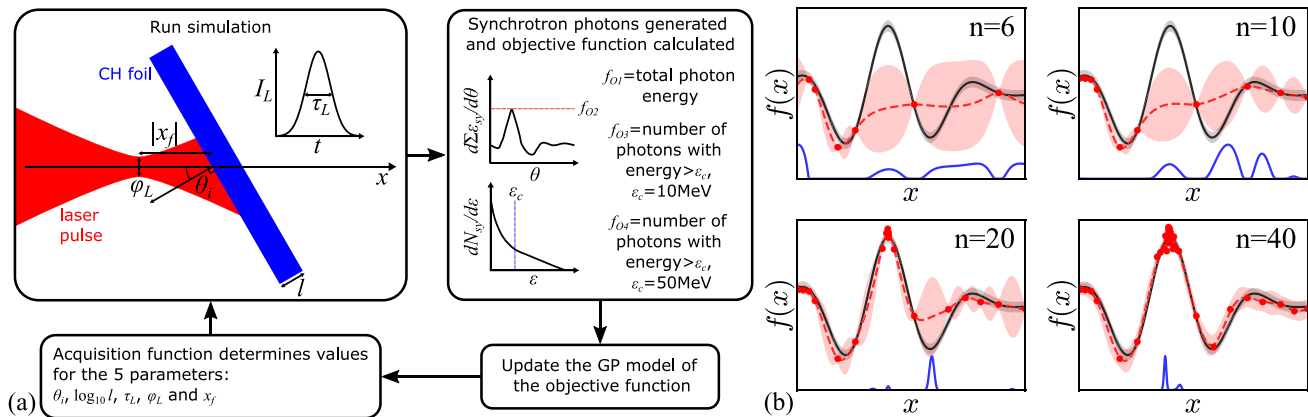


**Figure 1.** (a) The Bayesian optimization loop and schematic of the simulation setup. The synchrotron photon energy spectrum ( $dN_{sy}/d\varepsilon$ ) and angle-resolved yield ( $d\sum \varepsilon_{sy}/d\theta$ ) generated in each simulation are depicted to illustrate several of the objective functions. (b) An example of Bayesian optimization of a noisy 1D function showing the true function (black), the model (red) and the acquisition function (blue) for different numbers of iterations ( $n$ ).

were  $\theta_i$ ,  $\log_{10} I_L$ ,  $\tau_L$ ,  $\phi_L$  and  $x_f$ , illustrated in Figure 1(a). Several of the objective functions used (defined in Sections 4 and 5), which correspond to important parameters of the synchrotron emission, are also shown: the synchrotron yield, peak angle-resolved yield and number of photons in the high-energy spectral tail for different cut-off values. The optimum parameters found in Sections 4 and 5 generally match what is expected from the 2D parameter space scans in Section 3. An example demonstration of Bayesian optimization of an arbitrary 1D function susceptible to noise is shown in Figure 1(b) for different numbers of iterations.

Previously, the same approach was applied for the optimization of laser-driven ion acceleration<sup>[67]</sup> using a single physical parameter in the objective function (maximum ion energy). Here this method is applied both for single and multiple physical parameters in the objective function, enabling the exploration of different objective functions to influence the trade-off in one required beam parameter against another.

### 3. 2D parameter space scans of gamma ray emission

Before optimizing the interaction, the influence of a number of input parameters, including each of the chosen optimization parameters, was first explored in 2D parameter space scans. The target thickness was one of the varied parameters in each scan, enabling separation of the effect of RSIT, which can be controlled with target thickness<sup>[83]</sup>, from the effect of varying each of the other parameters. Initially, in Figures 2(a)–2(c) a pulse with  $\tau_L = 30$  fs,  $\phi_L = 3$   $\mu$ m and  $x_f = 0$  incident at target normal ( $\theta_i = 0^\circ$ ) was considered, and simulated for peak laser intensities  $I_L = 3.16 \times 10^{21}$ – $3.16 \times 10^{23}$  W cm<sup>-2</sup>, covering a range for which synchrotron radiation may become measurable, up to where it is expected to dominate. Target thicknesses between 50 nm and 5  $\mu$ m were simulated, encompassing relativistically transparent to

opaque targets across the intensity range, demonstrated by the percentage laser energy transmission in Figure 2(a) and also shown by the white contours of these values in Figures 2(a)–2(c).

To produce synchrotron radiation in these interactions, highly relativistic electrons are required in an intense electromagnetic field, and as changes to the target thickness cause a transition between transparent and opaque targets, the coupling of the laser energy to the electrons also changes<sup>[84]</sup>. Therefore, the total electron energy sampled along the  $x$ -axis ( $|y| < 6$  nm) in the transparent plasma in front of the relativistic critical density surface ( $x_c$ , where  $n_e = \gamma_e n_c$ ) and in the laser skin depth ( $\delta_s = c/\omega_{pe}$ ), integrated over the period of synchrotron emission (estimated as  $-\tau_L/2 < t < \tau_L$ , where the laser peak intensity reaches  $x = 0$  at  $t = 0$ ), was calculated for each of the simulations and is shown in Figure 2(b). The highest total electron energy in the plasma accessible to the laser field for each  $I_L$  simulated is on average found when the laser energy transmission is 13%, where the points either side of the maximum provide transmission bounds of 2.6% and 29%, respectively, for the maximum. This agrees well with the laser-to-synchrotron radiation energy conversion efficiency,  $\eta_{sy}$ , values in Figure 2(c), which are maximized for 11% transmission, with the adjacent points providing a range between 1.9% and 26%, indicating that the improved coupling of energy to electrons in the laser field for thin targets that undergo RSIT enhances the synchrotron conversion efficiency.

#### 3.1. Laser-injected synchrotron emission

For increasing  $I_L$ , the radiation pressure causes the critical surface to recede further in the interaction, forming a deeper cavity in the target. Electrons are pulled transversely towards the centre of the focal spot by the laser electric field as it interacts with the walls of the plasma cavity, with the electron trajectory and the side of the focal spot and target

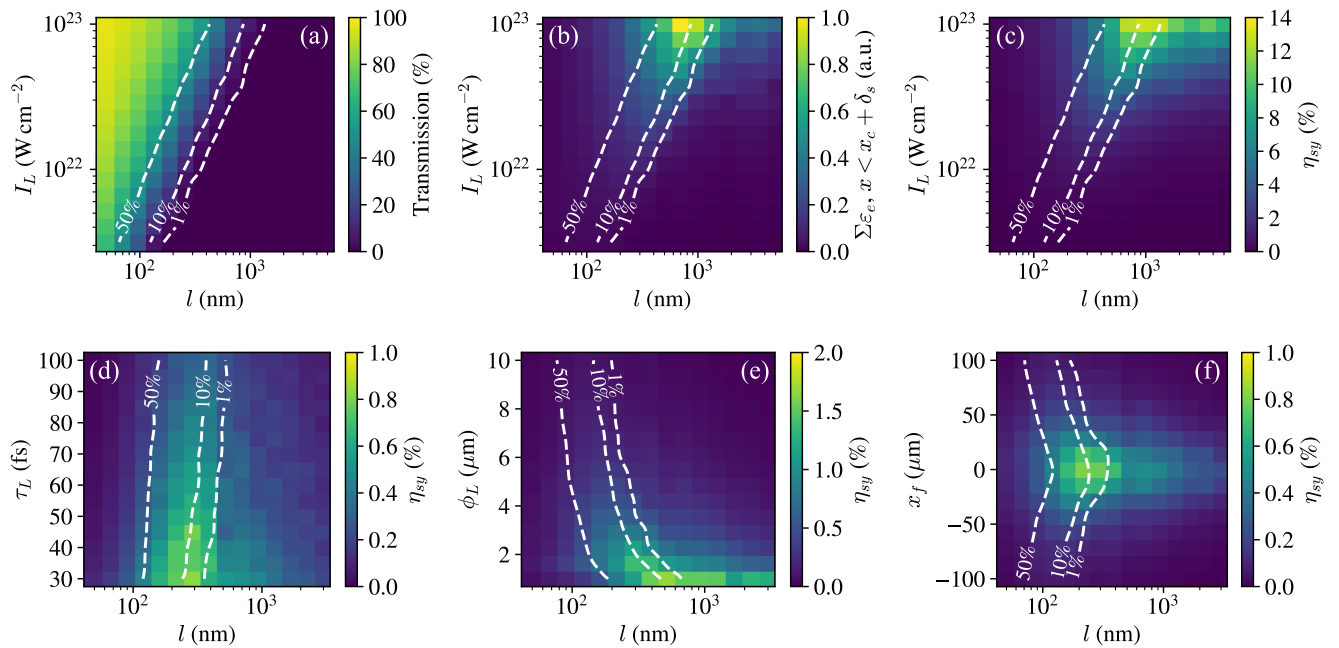


**Figure 2.** (a) Percentage transmission of the laser pulse, (b) total electron energy in front of the plasma critical surface and in the laser skin depth averaged over the period of synchrotron emission and (c) laser-to-synchrotron photon energy conversion efficiency, all for varying target thickness and laser intensity. (d)–(f) Laser-to-synchrotron photon energy conversion efficiency for varying pulse duration, focal spot size and defocus, respectively, with target thickness.

cavity the electrons are injected from determined by the instantaneous direction of the laser electric field as it oscillates, producing a large quantity of synchrotron gamma rays in two forward-propagating lobes. This laser-injected emission process is different from the edgeglow emission reported in Refs. [26,62], in which the transverse ponderomotive clearing of electrons by the laser pulse generates transverse space charge fields that reintroduce electrons into the channel formed in the target. The emergence of laser-injected emission due to hole boring<sup>[85,86]</sup> causes the conversion efficiency for opaque targets to approach the highest achievable with transparent targets at  $I_L \sim 10^{23} \text{ W cm}^{-2}$ .

### 3.2. Pulse duration, spot size and defocus

In Figures 2(d)–2(f), the synchrotron conversion efficiency is shown, where the laser energy is kept constant in the 2D simulation geometry corresponding to peak intensity  $I_L = 3 \times 10^{22} (30 \text{ fs}/\tau_L)(1 \mu\text{m}/\phi_L) \text{ W cm}^{-2}$  varying linearly with  $1/\phi_L$ . The values of the other parameters used are  $\tau_L = 30 \text{ fs}$ ,  $\phi_L = 3 \mu\text{m}$  and  $x_f = 0$ , unless scanned. The highest conversion efficiencies for Figures 2(d)–2(f) are on average found for laser transmission values of 10%, 11% and 15%, respectively, similar to the laser intensity scan results. The maximum conversion efficiencies in these scans are achieved for the minimum pulse duration, spot size and defocus, for each of which the laser intensity is maximized. Increasing the magnitude of defocus increases the beam width on the target surface, and in Figure 2(f) such changes exhibit similar results to variation of the spot

size in Figure 2(e), with  $\eta_{\text{sy}}$  independent of the direction of the defocus.

### 3.3. Stability

Although these results indicate that the most efficient synchrotron radiation source for a fixed laser pulse energy corresponds to the shortest pulse duration and smallest focal spot size focused onto the surface of a partially transmissive foil, the small Rayleigh length,  $z_R = \pi \phi_L^2 / 2\lambda_L \ln 2$ , for a near-wavelength  $\phi_L$  makes the interaction highly susceptible to small changes in the defocus. This was tested in 3D simulations, using the same configuration as in Section 7, for  $\phi_L = 1 \mu\text{m}$ ,  $I_L = 3 \times 10^{22} \text{ W cm}^{-2}$ , linear (along  $y$ ) polarization, normal incidence and one Rayleigh length,  $2.83 \mu\text{m}$ , of defocus. For  $x_f = 0$ ,  $z_R$  and  $-z_R$ , the synchrotron conversion efficiency is 15.0%, 20.8% and 3.0%, respectively, corresponding to changes of +39% and –80% for the positive and negative defocus, respectively. In addition, the rapid variation of  $\eta_{\text{sy}}$  with changes to the transmission also makes such a source susceptible to changes in the plasma expansion dynamics. If source stability is required, a larger than near-wavelength sized focal spot is recommended. If laser intensities of approximately  $10^{23} \text{ W cm}^{-2}$  are achievable,  $\eta_{\text{sy}}$  is more stable to changes in  $l$  for less than 10% transmissive targets due to the dominance of laser-injected synchrotron emission induced by hole boring of the target. This may be achievable for lower peak laser intensities if a lower density target material is used, or for solid targets with a preformed front surface structure, such as the concave targets modeled in Ref. [50].

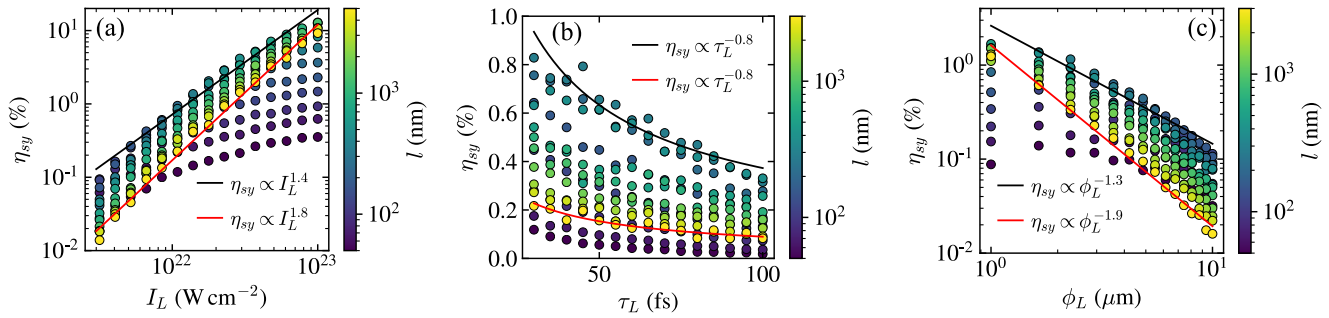


**Figure 3.** Scaling of the laser-to-synchrotron energy conversion efficiency with (a) peak laser intensity, (b) pulse duration and (c) focal spot FWHM, for varying target thickness. Power law fits are shown for the optimum target thicknesses (black) and for the thickest targets used (red;  $l = 5 \mu\text{m}$  for (a) and  $l = 3 \mu\text{m}$  for (b) and (c)).

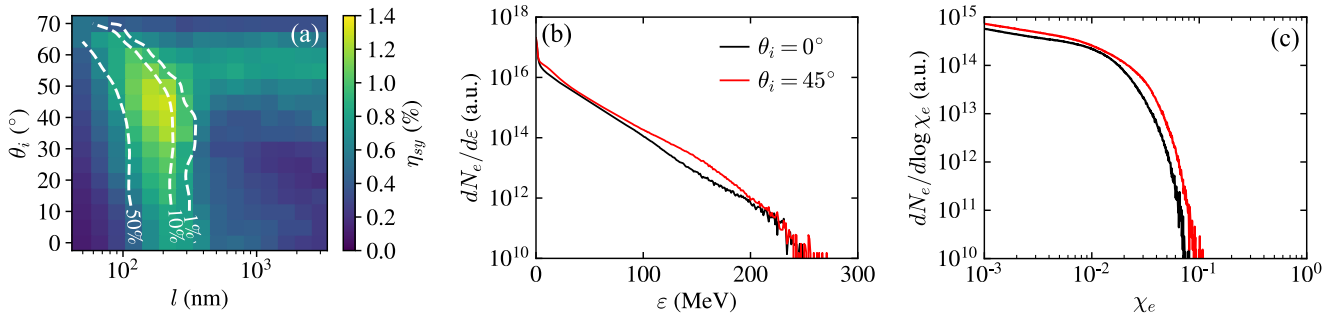


**Figure 4.** (a) Laser-to-synchrotron photon energy conversion efficiency for varying angle-of-incidence and target thickness. (b) Electron spectra, sampled over the whole simulation space, averaged over the period of synchrotron emission for a 200 nm foil at normal and  $45^\circ$  incidence, and (c) the corresponding time-averaged  $\chi_e$  spectra.

### 3.4. Scaling of the synchrotron conversion efficiency

The 2D parameter space scans provide target thickness-dependent scalings of  $\eta_{\text{sy}}$  with each of the other parameters. In Figure 3, these are presented for peak laser intensity, pulse duration and focal spot size, with power law fit values given for the value of  $l$  that maximizes  $\eta_{\text{sy}}$  (black line) and for an indicative opaque target (red line;  $l = 5 \mu\text{m}$  for Figure 3(a) and  $l = 3 \mu\text{m}$  for Figures 3(b) and 3(c)). In Figure 3(a),  $\eta_{\text{sy}} \propto I_L^{1.8}$  for  $l = 5 \mu\text{m}$  and  $\eta_{\text{sy}} \propto I_L^{1.4}$  for the optimum thicknesses, in agreement with the  $\eta_{\text{sy}} \propto I_L^{1.5}$  scalings reported in Refs. [27,57]. In both cases, the rate of increase slows as  $I_L$  approaches  $10^{23} \text{W cm}^{-2}$ . The faster scaling for  $l = 5 \mu\text{m}$  and the convergence of the two lines of fit in Figure 3(a) result from the reduced role of target expansion in the optimization of the synchrotron emission with increasing laser intensity, due to the increasing importance of the radiation pressure and the increasing relativistically corrected critical density.

The use of ultrathin targets can increase  $\eta_{\text{sy}}$  by almost an order of magnitude compared with  $l = 5 \mu\text{m}$  for the lowest intensities considered here, and therefore such targets provide the most accessible route to generating synchrotron radiation in laser–solid interactions. Synchrotron emission can be increased for the case of thick targets if the laser pulse interacts with a significant pre-plasma at the front surface, which can be produced by the laser light preceding the main pulse if the temporal-intensity contrast is low

enough. This was not modelled in our simulations, which only included the main Gaussian peak in the temporal profile of the laser pulse. In experiments, increasing the peak laser intensity by orders of magnitude may require increasing the temporal-intensity contrast to prevent pre-expansion of the target or the creation of a significant pre-plasma at the front surface. Otherwise, the optimum conditions for synchrotron generation are expected to change.

For constant laser pulse energy, the pulse duration is found to play a weaker role, with  $\eta_{\text{sy}} \propto \tau_L^{-0.8}$  for both  $l = 3 \mu\text{m}$  and the transparent optimum thicknesses in Figure 3(b). In contrast, the conversion efficiency depends strongly on  $\phi_L$ , with  $\eta_{\text{sy}} \propto \phi_L^{-1.9}$  for  $l = 3 \mu\text{m}$  and  $\eta_{\text{sy}} \propto \phi_L^{-1.3}$  for the optimum thicknesses in Figure 3(c). In a similar manner to the intensity scan, the transition from RESE-dominated synchrotron emission for  $\phi_L = 10 \mu\text{m}$  to laser-injection-dominated emission for  $\phi_L = 1 \mu\text{m}$  produces these different scalings. The faster  $I_L \propto \phi_L^{-2}$  dependence of the pulse intensity on the focal spot size in 3D for constant pulse energy may provide a different  $\eta_{\text{sy}}$  scaling with  $\phi_L$ .

### 3.5. Angle-of-incidence

The results for the final optimization parameter, the angle-of-incidence of the laser pulse on the target, are shown in Figure 4. In Figure 4(a), the synchrotron conversion efficiency is maximized for  $\theta_i = 45^\circ$  and  $l = 216 \text{nm}$ , where it is 60% higher than the maximum value reached for normal

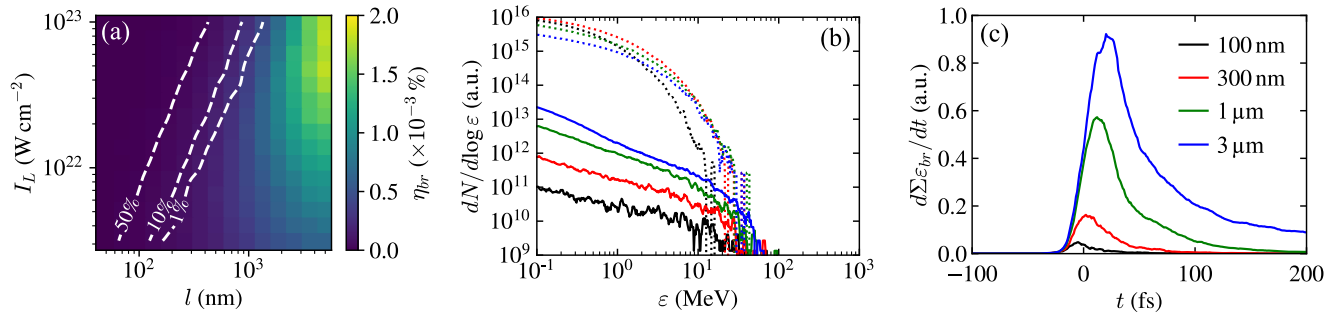


**Figure 5.** (a) Laser-to-bremsstrahlung radiation energy conversion efficiency for varying laser intensity and target thickness. (b) Energy spectra for bremsstrahlung photons (solid) and synchrotron photons (dotted) for different target thicknesses. (c) The rate of energy conversion to bremsstrahlung radiation.

incidence. Similar to the other parameters,  $\eta_{sy}$  is highest for targets that on average transmit 14% of the laser light. To explore why the angle-of-incidence improves  $\eta_{sy}$ , the electron energy spectra and  $\chi_e$  spectra (both averaged over the period of synchrotron emission) are plotted in Figures 4(b) and 4(c), respectively, for additional simulations using  $l = 200\text{ nm}$  and  $\theta_i = 0^\circ, 45^\circ$ . The fast electron population contains 36% more energy for  $\theta_i = 45^\circ$  compared with  $0^\circ$ , because the p-polarized light improves energy coupling to electrons, and a much larger number of electrons with energy greater than 100 MeV are produced. This contributes to the enhanced spectrum of  $\chi_e$  values, increasing the generation of synchrotron radiation.

### 3.6. Bremsstrahlung emission for varied laser intensity and target thickness

Until now, the discussion has focused on the generation of synchrotron radiation and how this depends on key laser and plasma parameters. Gamma radiation will, however, also be produced via bremsstrahlung emission in these interactions. Distinguishing between these two photon sources is important for the design of experiments that aim to investigate either mechanism.

In this investigation, thin foils of a low  $Z$  material have been selected to minimize the production of bremsstrahlung radiation. In Figure 5(a), the conversion efficiency to bremsstrahlung radiation,  $\eta_{br}$ , is shown for different values of the target thickness and peak laser intensity. Generally, the conversion efficiency is observed to increase with each of these parameters, except where the laser energy starts to be transmitted. In such targets the bremsstrahlung emission is expected to decrease due to the increased loss of fast electrons and the reduced absorption of the pulse into electrons as the transmission becomes large.

In Figure 5(b), the energy spectra of the bremsstrahlung and synchrotron radiation are shown for various target thicknesses, where  $I_L = 10^{22}\text{ W cm}^{-2}$ . In all cases, the synchrotron radiation dominates by many orders of magnitude. The conversion efficiency to synchrotron radiation scales

very quickly with peak laser intensity, and therefore the difference is expected to become even greater for higher intensities. The bremsstrahlung emission can take place for many picoseconds in laser–solid interactions<sup>[58]</sup>, due to the presence of a hot electron population trapped inside the target<sup>[87]</sup>. However, in Figure 5(c), the rate of energy conversion to bremsstrahlung radiation,  $d\sum \varepsilon_{br}/dt$ , where  $\varepsilon_{br}$  is the bremsstrahlung photon energy, for different target thicknesses is shown to quickly reduce after the peak of the laser temporal profile reaches the target at  $t = 0$ . Only for the thickest target tested,  $l = 3\ \mu\text{m}$  does the emission rate remain noticeable at the end of the simulation, and extrapolating this for a further 6 ps (the longest duration of  $K_\alpha$  emission measured in Ref. [87]) increases  $\eta_{br}$  from  $1.0 \times 10^{-3}\%$  to  $8.6 \times 10^{-3}\%$ . This is still dominated by the corresponding value of  $\eta_{sy} = 0.27\%$ . Our modelling captures the brightest period of bremsstrahlung emission, enabling us to find parameters that minimize its production whilst maximizing properties of the synchrotron emission, informing the design of experiments to generate the purest source and clearest signature of synchrotron radiation.

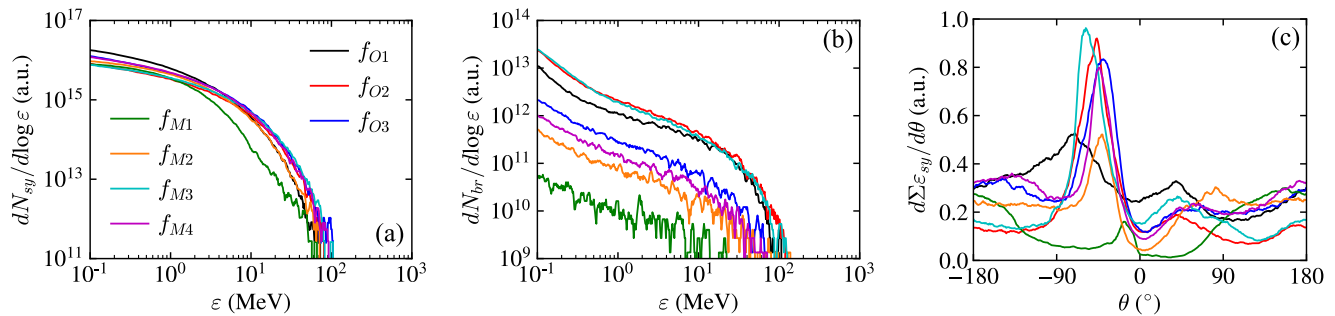
## 4. Application of Bayesian optimization

The scans discussed thus far vary only two input parameters at a time, over a  $15 \times 15$  grid corresponding to 225 simulations. To perform a systematic grid scan of this type with 15 values for each of the five input parameters under consideration would require  $15^5 = 759,375$  simulations, which was not feasible with the computational resources available. Instead, GP regression was used to identify the values of the input parameters that maximize a given objective function within 200 simulations.

The parameter search space was defined as  $0^\circ \leq \theta_i \leq 70^\circ$ ,  $50\text{ nm} \leq l \leq 10\ \mu\text{m}$ ,  $30\text{ fs} \leq \tau_L \leq 100\text{ fs}$ ,  $1\ \mu\text{m} \leq \phi_L \leq 6\ \mu\text{m}$  and  $-50\ \mu\text{m} \leq x_f \leq 50\ \mu\text{m}$ . The laser energy was kept constant in the same way as in the previous section, by setting  $I_L = 3 \times 10^{22} (30\text{ fs}/\tau_L) (1\ \mu\text{m}/\phi_L)\text{ W cm}^{-2}$ . The objective functions used are shown in Table 1, with the values of the input parameters for their optima. The objective functions

**Table 1.** The objective functions maximized with Bayesian optimization and the parameters of the found optimum for each.

Objective function	Parameter values at optimum				
	$\theta_i$ ( $^\circ$ )	$\log_{10}(l[\text{m}])$	$\tau_L$ (fs)	$\phi_L$ ( $\mu\text{m}$ )	$x_f$ ( $\mu\text{m}$ )
$f_{O1} = \sum \varepsilon_{\text{sy}}$	41.1	-5	42.8	1	0.7
$f_{O2} = \max(d \sum \varepsilon_{\text{sy}}/d\theta)$	26.4	-5	30	1	0.57
$f_{O3} = N_{\text{sy}}, \varepsilon_{\text{sy}} > 10 \text{ MeV}$	24.4	-6.26	30	1	0.63
$f_{M1} = f_{O2} / \sum \varepsilon_{\text{br}}$	70	-7.3	30	1	-4.33
$f_{M2} = A(f_{O2})f_{O2} / \sum \varepsilon_{\text{br}}$	40.6	-6.64	30	1	0.14
$f_{M3} = f_{O2}f_{O3}$	18.3	-5.23	30	1	0.85
$f_{M4} = f_{O2}f_{O3} / \sum \varepsilon_{\text{br}}$	30.9	-6.45	30	1	0.92

**Figure 6.** Synchrotron and bremsstrahlung radiation for the objective function optima in Table 1, for which  $I_L = 3 \times 10^{22} (30 \text{ fs}/\tau_L)(1 \mu\text{m}/\phi_L) \text{ W cm}^{-2}$ . (a) Synchrotron photon energy spectra, (b) bremsstrahlung photon energy spectra and (c) angular profiles of total emitted synchrotron photon energy.

that include only one physical property of the photon emission are as follows: the total energy of synchrotron emission ( $f_{O1}$ ), where  $\varepsilon_{\text{sy}}$  is the synchrotron photon energy; the maximum of the angle-resolved energy of synchrotron emission,  $d \sum \varepsilon_{\text{sy}}/d\theta$  ( $f_{O2}$ ), where  $\theta$  is the angle in the  $xy$ -plane from the positive  $x$ -axis; and the total number of synchrotron photons,  $N_{\text{sy}}$ , with energy exceeding 10 MeV ( $f_{O3}$ ).

To optimize multiple properties of the photon emission, a series of different objective functions were considered. These include the ratio of the peak angle-resolved energy of synchrotron emission to the total bremsstrahlung radiation energy ( $f_{M1}$ ), and the same function multiplied by the acceptance function  $A(f_{O2})$  ( $f_{M2}$ ). The acceptance function is defined as  $A(f) = 1/(1 + \exp(-(20/f_{\text{max}})(f - 0.5f_{\text{max}})))$ , where  $f$  is a given objective function and  $f_{\text{max}}$  is the maximum value of the objective function found separately in a previous optimization scan. The acceptance function strongly reduces the value of the overall function for  $f < f_{\text{max}}/2$  to guide the optimization towards results where  $f > f_{\text{max}}/2$ , and it is plotted in the [Supplementary Materials](#). In addition, the product of the peak angle-resolved energy of synchrotron emission and the number of synchrotron photons above 10 MeV ( $f_{M3}$ ), and this function divided by the total bremsstrahlung radiation energy ( $f_{M4}$ ), were optimized.

#### 4.1. Optimization of individual synchrotron emission properties

The resulting synchrotron and bremsstrahlung photon energy spectra and the angle-resolved energy of synchrotron

radiation are shown in [Figures 6\(a\)–6\(c\)](#), respectively, for the optimum of each objective function. In maximizing the total energy of synchrotron radiation with  $f_{O1}$ , the synchrotron spectrum with the highest number of photons less than 2 MeV is produced; such photons require less electron energy to be generated and thus can be generated in such high numbers to dominate the total synchrotron energy, accounting for 54% for  $f_{O1}$ . This also corresponds to the only optimum where the pulse duration is greater than the minimum of 30 fs, at 42.8 fs. In optimizing the maximum of  $d \sum \varepsilon_{\text{sy}}/d\theta$  and the number of synchrotron photons with energy greater than 10 MeV, similar peaks in  $d \sum \varepsilon_{\text{sy}}/d\theta$  at  $\theta \approx -50^\circ$  are found in [Figure 6\(c\)](#). The angular profiles differ mainly by the energy emitted in the backward direction ( $|\theta| > 90^\circ$ ) due to the dependency of the RESE mechanism on target thickness, enhanced for  $f_{O3}$ . The optimum for  $f_{O1}$  only reaches approximately half of the peak value of  $d \sum \varepsilon_{\text{sy}}/d\theta$  compared with  $f_{O2}$  and  $f_{O3}$ . The only sizeable difference in the parameters here, besides the small increase in  $\tau_L$ , is the change from  $\theta_i = 41.1^\circ$  to  $\theta_i \approx 25^\circ$ . The production of more directional synchrotron emission with changes to the angle-of-incidence has been reported in Refs. [31,46,88], in which a single lobe structure is also reported.

#### 4.2. Mitigation of the bremsstrahlung emission

In maximizing the ratio of the directional energy of synchrotron emission to the bremsstrahlung emission for  $f_{M1}$ , the bremsstrahlung has been strongly suppressed, as shown in [Figure 6\(b\)](#), at the cost of reducing the

peak value of  $d\sum \varepsilon_{sy}/d\theta$  and the synchrotron spectrum in Figure 6(a). The optimum parameters here in Table 1 correspond to the maximum possible angle-of-incidence and minimum target thickness. The optimization of the objective function has been dominated by the gains obtained by reducing the bremsstrahlung emission as much as possible. The optimum found, however, has synchrotron radiation dominated by emission in the backward direction ( $|\theta| > 90^\circ$ ) corresponding to RESE, unlike the stronger forward-directed ( $|\theta| < 90^\circ$ ) emission found with the other objective functions. Including the acceptance function with  $f_{M2}$ , an optimum with greater bremsstrahlung emission is found. However, a much higher peak value of  $d\sum \varepsilon_{sy}/d\theta$  is obtained, as shown in Figure 6(c). The use of an acceptance function here demonstrates a method of setting an acceptable limit on the trade-off in one of the physical properties included in a composite objective function in optimizing the overall function.

The objective functions  $f_{O2}$  and  $f_{O3}$  are already optimized for similar parameters, and in optimizing their product  $f_{M3}$ , similar optimum parameters and photon properties were found at the optimum, as shown in Figure 6. Optimization of this product divided by the total bremsstrahlung emission using  $f_{M4}$  effectively reduces the weight of the bremsstrahlung reduction term in comparison with  $f_{M1}$ , and produces photon distributions close to the  $f_{O2}$ ,  $f_{O3}$  and  $f_{M3}$  optima with much less bremsstrahlung emission. This optimum is at a different location in the parameter space to the previous efforts to reduce the bremsstrahlung emission ( $f_{M1}$  and  $f_{M2}$ ), and in a different part of the objective space, some increase to bremsstrahlung emission has enabled stronger synchrotron emission to be generated.

### 4.3. Intensity

For all of these optimization results, the best spot size corresponds to the minimum,  $\phi_L = 1 \mu\text{m}$ . In most cases the pulse duration also corresponds to the minimum,  $\tau_L = 30\text{fs}$ . Also, in most cases, the defocus is approximately  $0.6 \mu\text{m}$ , shifting the laser focus close to the new critical surface position after the initial hole boring. The objective functions used here for improving synchrotron radiation are almost universally optimized for the highest on-target intensity.

## 5. Optimization in the synchrotron dominated regime

The optimization results discussed thus far are for conditions in which the synchrotron emission is relatively weak. The laser energy was increased by a factor of 10, corresponding to  $I_L = 3 \times 10^{23} (30\text{fs}/\tau_L) (1 \mu\text{m}/\phi_L) \text{W cm}^{-2}$  for which the synchrotron emission is expected to become extremely strong, and further optimization scans were performed to identify the impact on the optimum input parameters. The objective functions  $f_{O1}$ ,  $f_{O2}$ ,  $f_{M1}$  and  $f_{M2}$  were used again. Instead of  $f_{O3}$ , the total number of synchrotron photons with energy above 50 MeV ( $f_{O4}$ ) is optimized, due to the higher energy photon spectra produced under these conditions. Similar optimum parameters were obtained, as listed in Table 2, with the highest intensity combination of  $\tau_L$ ,  $\phi_L$  and  $x_f$  values for most objective functions. An optimum defocus of close to  $2 \mu\text{m}$  is found for objective functions  $f_{O1}$ ,  $f_{O2}$  and  $f_{O4}$ , several times greater than the lower intensity cases in Table 1. This is due to the increased hole boring velocity, induced by the higher laser intensity, leading to greater recession of the critical surface at the target front side.

### 5.1. Angle-resolved synchrotron emission

The optimum of  $f_{O2}$  corresponds to the maximum pulse duration of 100fs. Similar peak values of  $d\sum \varepsilon_{sy}/d\theta$  were obtained across the permitted range of values for the pulse duration. However, the direction of peak emission moves from  $\theta \approx -50^\circ$  for  $\tau_L \approx 30\text{fs}$  to  $\theta \approx 0^\circ$  for  $\tau_L \approx 100\text{fs}$ . Emission in the same direction as the laser pulse propagation ( $\theta = 0^\circ$ ) has previously been associated with skin depth emission from the electrons near the front of the laser pulse in the reflected light<sup>[26,62]</sup>. However, the peak in the angle-resolved emission for the optimum of  $f_{O2}$  is a result of the stronger deformation of the target for the longer pulse duration. A deeper cavity in the target is formed, and electrons injected into the laser pulse from the edge of the cavity on the  $y > 0$  side of the focal spot by the positive half-cycle of the laser electric field are caught up by the next half-cycle of the laser pulse as they propagate. The change in the direction of the laser electric field experienced by the injected electrons forces them to propagate close to parallel with the laser pulse, emitting in this direction. In comparison

**Table 2.** The objective functions used for optimization with laser intensity of  $3 \times 10^{23} (30\text{fs}/\tau_L) (1 \mu\text{m}/\phi_L) \text{W cm}^{-2}$ , and the parameters of the found optima.

Objective function	Parameter values at optimum				
	$\theta_i$ ( $^\circ$ )	$\log_{10}(I[\text{m}])$	$\tau_L$ (fs)	$\phi_L$ ( $\mu\text{m}$ )	$x_f$ ( $\mu\text{m}$ )
$f_{O1} = \sum \varepsilon_{sy}$	38	-5.6	30	1	1.76
$f_{O2} = \max(d\sum \varepsilon_{sy}/d\theta)$	45.6	-5	100	1	1.93
$f_{O4} = N_{sy, \varepsilon_{sy} > 50 \text{ MeV}}$	0	-5.22	30	1	1.89
$f_{M1} = f_{O2} / \sum \varepsilon_{br}$	70	-7.3	30	5.33	-50
$f_{M2} = A(f_{O2})f_{O2} / \sum \varepsilon_{br}$	54.3	-5.91	30	1	0.19

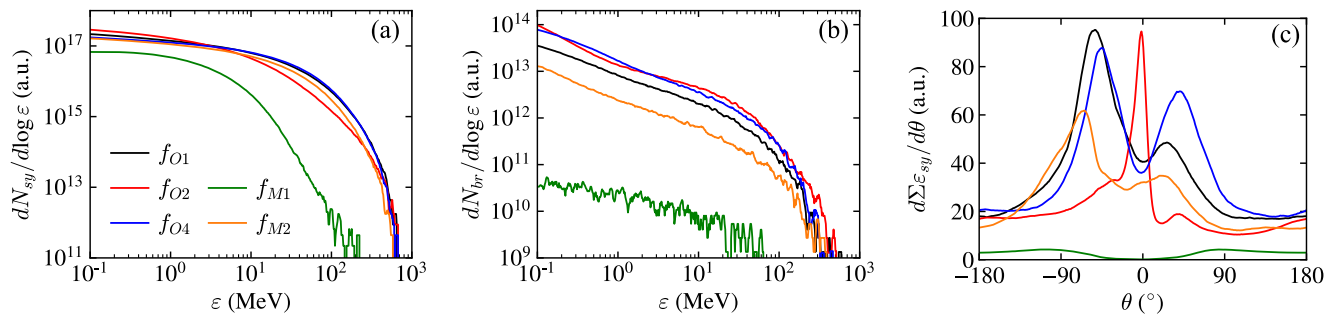


**Figure 7.** Synchrotron and bremsstrahlung radiation for the objective function optima in Table 2, for which  $I_L = 3 \times 10^{23} (30 \text{ fs}/\tau_L)(1 \mu\text{m}/\phi_L) \text{ W cm}^{-2}$ . (a) Synchrotron photon energy spectra, (b) bremsstrahlung photon energy spectra and (c) angular profiles of total emitted synchrotron photon energy.

with the lower laser intensity case in Figure 6(c), with the same normalization constant, a  $100\times$  enhancement in the peak value is obtained for only a  $10\times$  higher energy laser pulse. Although the maximum synchrotron photon energies obtained for this optimum set of parameters are similar to the other spectra in Figure 7(a), the spectrum is shifted to lower photon energies, containing the most radiation below 2 MeV.

Optimization of total synchrotron emission with  $f_{O1}$  produces a peak in the angle-resolved synchrotron emission of similar magnitude to the optimum for  $f_{O2}$  in Figure 7(c), inadvertently maximizing both objectives. This optimum exhibits a pronounced double-peaked structure in the angular emission characteristic of synchrotron radiation from solid targets<sup>[26–28,32,57,62]</sup>. However, the  $38^\circ$  angle-of-incidence has resulted in the suppression of the lobe in the direction closer to the perpendicular of the rotated target surface and the enhancement of the lobe closer to the parallel. This behaviour is also present in Figure 6(c), although the weakened lobe is less discernible due to the more comparable backward-directed radiation. The effect of varying the angle-of-incidence on the synchrotron angular profile is discussed in more detail in the following sections. The optimum for  $f_{O1}$  also produces a near-identical synchrotron spectrum to that for  $f_{O4}$ , where the high-energy spectral tail is optimized with a thicker target and normal incidence.

## 5.2. Mitigation of the bremsstrahlung emission

The optimum parameters to reduce bremsstrahlung radiation whilst maximizing angle-resolved synchrotron emission for  $f_{M1}$  still correspond to the minimum target thickness (50 nm) and maximum angle-of-incidence ( $70^\circ$ ). However, in this case the optimum occurs for the largest possible defocus,  $x_f = -50 \mu\text{m}$ , and almost the maximum spot size,  $\phi_L = 5.33 \mu\text{m}$ . Irradiating such an ultrathin target with the minimum possible beam width results in the foil rapidly expanding, becoming transparent very early in the interaction and reducing coupling into synchrotron radiation. Increasing the beam size on the target increases the target volume that the laser pulse interacts with, at the cost

of reduced laser intensity. A larger  $\phi_L$  also increases the Rayleigh length, extending the longitudinal distance over which synchrotron radiation is produced. This enhances the overall synchrotron emission faster than any potential increase to the bremsstrahlung emission. The faster increase of bremsstrahlung emission compared with synchrotron emission with thicker targets always leads to the thinnest targets maximizing their ratio.

The angle-resolved synchrotron emission for the optimum of  $f_{M1}$  in Figure 7(c) is maximized for  $|\theta| \approx 90^\circ$ , in contrast to the lower laser pulse energy case in Figure 6(c), which peaks for  $|\theta| \approx 180^\circ$ . The objective function  $f_{M2}$  that includes an acceptance function to guide the optimization towards results above a threshold value for  $f_{O2}$  is used again for the higher laser energy case, and demonstrates a successful increase to the peak angle-resolved synchrotron emission in Figure 7(c), with much higher bremsstrahlung emission, as shown in Figure 7(b).

The optimization results found here indicate the need to maximize the laser intensity interacting with the surface of solid targets to produce the strongest sources of synchrotron radiation. Rotation of the target in the plane of polarization of the laser pulse can produce the highest peak angle-resolved synchrotron emission, and the use of ultrathin foils is a very effective method of reducing the bremsstrahlung emission to generate a purer source of synchrotron emission. The optimization of multiple objectives in a single objective function can be effectively controlled with careful definition of the objective function, and use of such methods is demonstrated to generate comparable to best-case synchrotron emission in sub- $\mu\text{m}$  foils where the bremsstrahlung emission is still strongly mitigated.

## 6. Angle-of-incidence dependence of the forward synchrotron emission

Through applying Bayesian optimization, the angle-of-incidence has been identified as a critical parameter influencing the spatial profile of the synchrotron emission. This was investigated in more detail using laser parameters

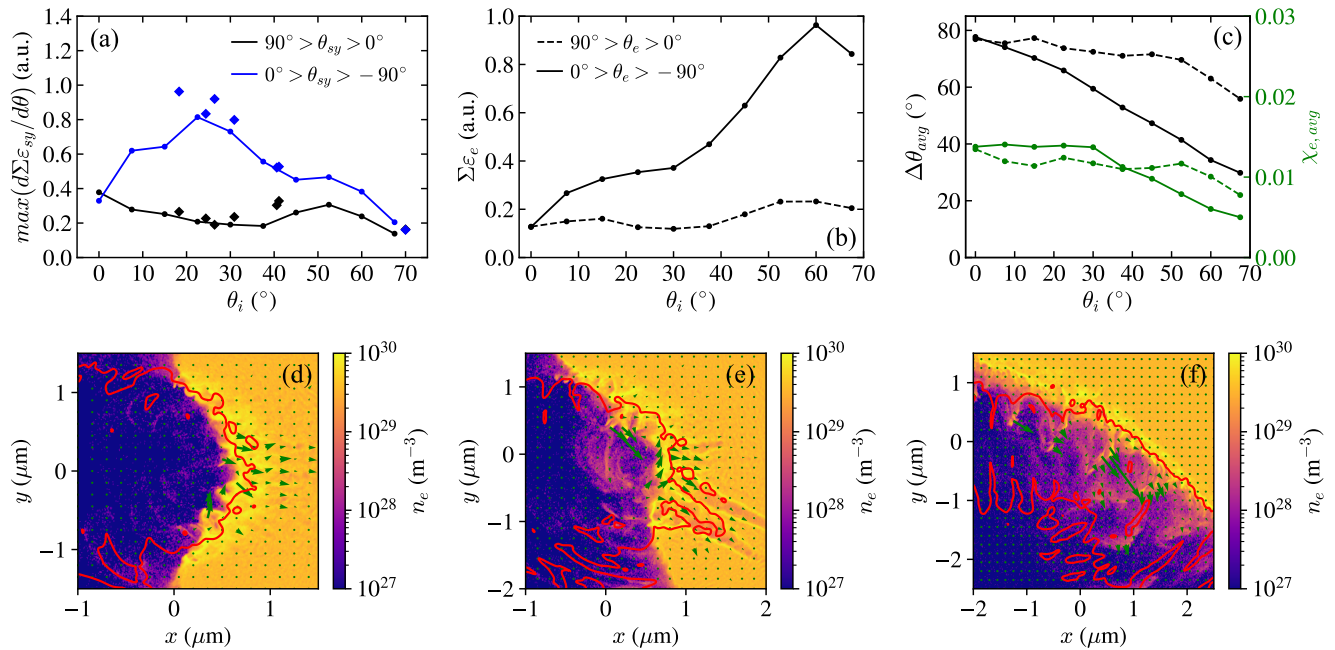


**Figure 8.** (a) Maximum value of  $d \sum \varepsilon_{sy}/d\theta$  as a function of the angle-of-incidence for synchrotron photons emitted in angular ranges  $\theta_{90,0}$  (black) and  $\theta_{0,-90}$  (blue), where  $l = 3 \mu\text{m}$ ,  $I_L = 3 \times 10^{22} \text{ W cm}^{-2}$ ,  $\phi_L = 1 \mu\text{m}$ ,  $\tau_L = 30 \text{ fs}$  and  $x_f = 0$ . The optima in Figure 6 are also shown (diamonds). (b) Total energy in electrons more than 10 MeV in a local intensity more than  $10^{21} \text{ W cm}^{-2}$  propagating with angle  $\theta_e$  in the ranges  $\theta_{90,0}$  (dashed) and  $\theta_{0,-90}$  (solid) averaged over the period of synchrotron emission. (c) Energy-weighted mean angle between the electron trajectory and the propagation direction of the local electromagnetic field (left-hand axis) and mean electron quantum parameter (right-hand axis) for each group of electrons in (b). (d)–(f) The electron density for  $\theta_i = 0^\circ$ ,  $22.5^\circ$  and  $60^\circ$ , respectively, where the total momentum of fast electrons (arrows) and the  $I = 10^{21} \text{ W cm}^{-2}$  contour (red) are also shown.

$I_L = 3 \times 10^{22} \text{ W cm}^{-2}$ ,  $\tau_L = 30 \text{ fs}$ ,  $\phi_L = 1 \mu\text{m}$  and  $x_f = 0$  (close to most of the optima) and  $l = 3 \mu\text{m}$  (an arbitrary thickness opaque target).

In Figure 8(a), the maximum value of  $d \sum \varepsilon_{sy}/d\theta$  is shown for different directions of the emitted synchrotron photons,  $\theta_{sy}$ , as a function of the angle-of-incidence. The photons are grouped into those propagating with direction  $90^\circ > \theta_{sy} > 0^\circ$  and  $0^\circ > \theta_{sy} > -90^\circ$ , corresponding to the directions in which the two lobes are usually produced due to laser-injected emission; these directions are hereafter referred to as  $\theta_{90,0}$  and  $\theta_{0,-90}$  for brevity. The optimization results from Table 1 and Figure 6(c) are added as data points. The observed lobes are of similar magnitude for normal incidence. As the target is rotated to give the normal to the front surface direction  $\theta_n = \theta_i - 180^\circ$ , the magnitude of the lobe propagating in  $\theta_{0,-90}$  (closer to parallel with the target surface) is enhanced by more than a factor of two when it peaks for  $\theta_i = 22.5^\circ$ . Many of the Bayesian optimization results are for similar values of  $\theta_i$ , albeit with greater directional synchrotron emission achieved due to changes to some of the parameters and many iterations. At the same time the magnitude of the  $\theta_{90,0}$ -directed emission is reduced, and this begins to reverse for  $\theta_i = 37.5^\circ$ – $52.5^\circ$  until the emission in both directions shown reduces in magnitude and begins to converge for increasing  $\theta_i$ .

The synchrotron radiation is caused by highly relativistic electrons within the laser field, and the direction of the

emitted radiation is predominantly in the electron direction of motion,  $\theta_e$ . The effect of varying the angle-of-incidence is examined by considering the electrons with energy greater than 10 MeV in local electromagnetic fields with intensity greater than  $10^{21} \text{ W cm}^{-2}$ . The total energy of such electrons propagating in the same direction as each of the synchrotron lobes is averaged over the period of synchrotron emission and is shown in Figure 8(b). For normal incidence, the total electron energy in each direction is equal, and as the target is rotated, the electron population that propagates in the  $\theta_{0,-90}$  direction rapidly acquires several times more total energy and continues to gain energy until  $\theta_i = 60^\circ$ . By contrast, the total energy of the electron population that propagates in the  $\theta_{90,0}$  direction over the interaction changes very little with  $\theta_i$ , with a minimum for  $\theta_i \approx 30^\circ$  and a second peak at  $\theta_i \approx 52.5^\circ$ . Although these changes match some of those for the peak angle-resolved synchrotron emission in Figure 8(a), they do not explain why the  $\theta_{0,-90}$ -directed emission peaks for  $\theta_i = 22.5^\circ$  and why the peak emission in both directions reduces for  $\theta_i$  approaching  $70^\circ$ .

The equation for  $\chi_e$  indicates that the synchrotron emission increases for increasing  $\gamma_e$  and for increasing  $\mathbf{E}_\perp + \mathbf{v}_e \times \mathbf{B}$ . The orientation of the electron motion to the fields,  $\Delta\theta$ , is therefore important to consider. Here,  $\chi_e$  is maximized for antiparallel propagation  $\Delta\theta = 180^\circ$  and minimized for parallel propagation  $\Delta\theta = 0^\circ$ . Figure 8(c) shows the energy-weighted average absolute angle between the direction of

motion of the electrons and the local electromagnetic field, calculated from the Poynting vector  $\mathbf{S} = \mathbf{E} \times \mathbf{B}/\mu_0$ . For the  $\theta_{0,-90}$ -propagating electron population, the average angle between the electrons and the field exhibits an approximately linear decrease from  $\theta_i = 0^\circ$  to  $70^\circ$ . For the same field magnitude and  $\gamma_e$ , this would reduce the synchrotron radiation. The energy-weighted average value of  $\chi_e$  for the electrons propagating in each direction is also shown in Figure 8(c), where it can be seen that  $\chi_{e,\text{avg}}$  changes very little for  $\theta_i = 0^\circ$ – $30^\circ$ , but is strongly reduced for greater  $\theta_i$ . The optimization of the magnitude of the angle-resolved synchrotron emission in  $\theta_{0,-90}$  is a result of the balance of the greater energy in the population of electrons propagating in the same direction with the reduced average emission parameter. For the  $\theta_{90,0}$ -directed electron population, the angle to the field  $\Delta\theta$  and the average emission parameter  $\chi_{e,\text{avg}}$  only begin to strongly reduce for  $\theta_i > 52.5^\circ$ , which reflects the behaviour of the associated synchrotron emission in Figure 8(a).

Example snapshots of the electron density on the simulation grid are shown in Figures 8(d)–8(f) close to the time of peak synchrotron emission for  $\theta_i = 0^\circ$ ,  $22.5^\circ$  and  $60^\circ$ , respectively. The red contours correspond to  $I = 10^{21} \text{ W cm}^{-2}$ , and the arrows show the total momentum of fast electrons in each  $150 \text{ nm} \times 150 \text{ nm}$  region. For normal incidence in Figure 8(d), in every half laser cycle the electric field pulls electrons from one side of the focal spot towards the centre, with the electrons periodically coming from the different sides of the focal spot due to the oscillating direction of the laser electric field. This results in periodic synchrotron radiation at the laser frequency with the lobes separated by half a laser cycle, as observed in Ref. [28]. The shallow depth of the front surface plasma cavity means that only electrons propagating at a steep angle with the incoming laser pulse move into and experience the highest fields.

When the target is rotated to  $\theta_i = 22.5^\circ$ , as in Figure 8(b), the laser fields can pull electrons from a greater area and along the surface of the target further forwards with the pulse. This enhances the coupling of laser energy to  $\theta_{0,-90}$ -propagating electrons, and as a result enhances the synchrotron emission in this direction. When  $\theta_i$  is increased further to  $60^\circ$ , as shown in Figure 8(c), the laser pulse is no longer reflected back in the  $|\theta| > 90^\circ$  direction, but along the surface of the target, reducing enhancement of the synchrotron radiation from counter-propagation of the reflected light with the laser-injected electrons propagating along the target surface. These electrons move with the laser pulse, which reduces their values of  $\chi_e$ , as shown in Figure 8(c), and causes them to produce less synchrotron radiation.

The Bayesian optimization results in Table 2 and Figure 7(c) indicate a laser intensity dependence of the optimum angle-of-incidence for producing the highest peak angle-resolved synchrotron emission, with the best results for  $\theta_i \approx 42^\circ$  in comparison with  $\theta_i \approx 25^\circ$  for the lower

laser intensity case. The hole boring velocity increases for increasing laser intensity, causing the formation of a deeper cavity in the target and changing the evolution of the geometry of the interaction, and hence the optimum value of  $\theta_i$ . The hole boring velocity also reduces for higher densities. The optimum value of  $\theta_i$  is therefore also expected to be dependent on the target density.

## 7. Spatial control of synchrotron emission in 3D simulations

The investigation of the angle-of-incidence, which is highly influential on the spatial profile of synchrotron emission, identified through the optimization scans and explored in 2D in the previous section, was extended with 3D simulations. The synchrotron emission is dominated by electrons accelerated and injected from the edges further into the laser spatial profile due to interaction with the laser electric field, and therefore the spatial profile of synchrotron emission should change as the polarization of the laser light changes. This motivates simulations in which we separately test the effect of p-, s-, left-hand c- and right-hand c- polarized laser light on the spatial profile of synchrotron emission for varying angle-of-incidence.

A lower plasma density of  $100n_c$  was simulated due to the high computational resources required to model higher plasma densities accurately in 3D. This may produce differences in the variation of the laser-injected synchrotron emission with the angle-of-incidence, as discussed at the end of the previous section. A single target thickness of  $1 \mu\text{m}$  was chosen, due to the increased resources required to simulate thicker targets. Therefore, the synchrotron emission was not optimized with target thickness (or transparency) for each angle-of-incidence tested. Transparency occurs for each polarization state at normal incidence, eventually becoming opaque as the angle-of-incidence is increased, and is polarization dependent. The laser parameters were  $I_L = 3 \times 10^{22} \text{ W cm}^{-2}$ ,  $\tau_L = 30 \text{ fs}$ ,  $\phi_L = 1 \mu\text{m}$  and  $x_f = 0$ , corresponding to a pulse energy of  $10.9 \text{ J}$ .

The spatial profiles of synchrotron emission are shown as a function of  $\theta$ , the azimuthal angle from the positive  $x$ -axis in the  $xy$  plane where  $-180^\circ \leq \theta \leq 180^\circ$ , and  $\phi$ , the polar angle from the positive  $z$ -axis where  $0^\circ \leq \phi \leq 180^\circ$ . The angle-of-incidence corresponds to rotation in the  $xy$  plane as in the 2D simulations.

Figure 9(a) shows the maximum angle-resolved energy of synchrotron emission of the two azimuthally defined regions corresponding to  $\theta_{90,0}$  and  $\theta_{0,-90}$ , as in the 2D results, as a function of the angle-of-incidence for p-polarization. In a similar manner to the 2D results, the magnitude of the emission in each direction for near-normal incidence is approximately equal. For increasing values of  $\theta_i$ , the magnitude of the  $\theta_{90,0}$ -directed emission drops very rapidly, and the magnitude of the  $\theta_{0,-90}$ -directed emission achieves

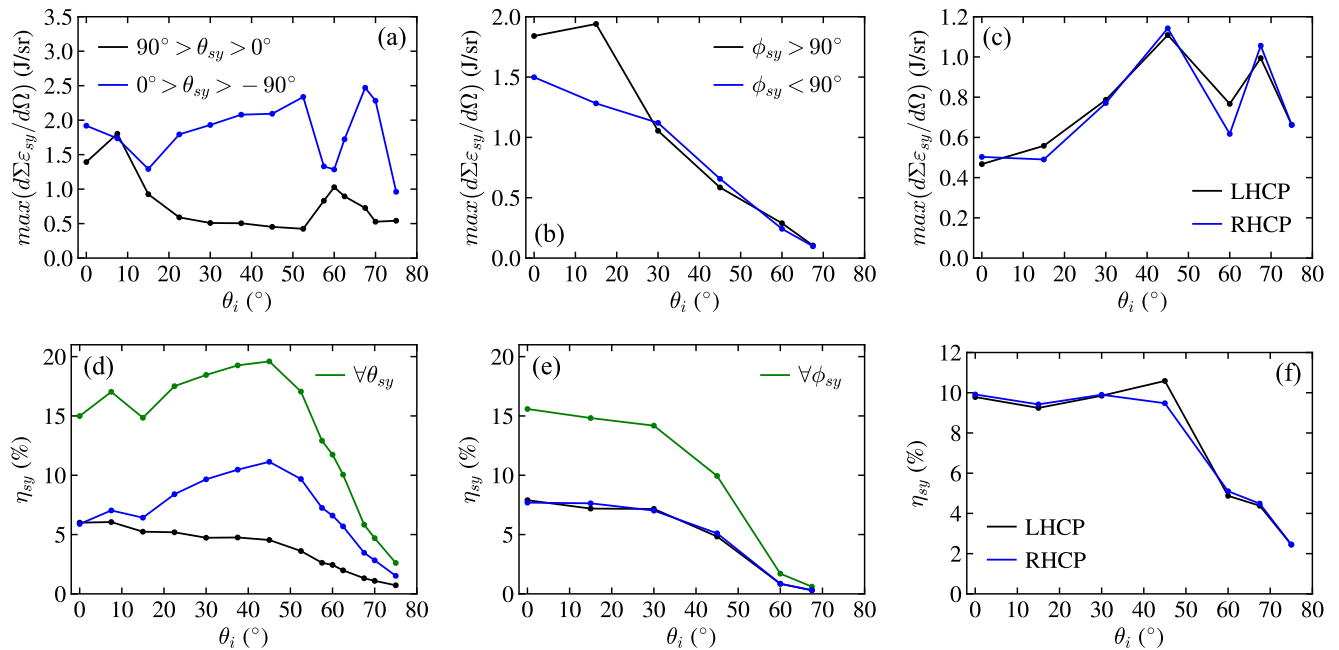


**Figure 9.** 3D simulation results for synchrotron photon emission for different laser light polarization states. Peak angle-resolved synchrotron energy emitted in each direction for (a) p-polarization, (b) s-polarization and (c) left-hand and right-hand circular polarization. (d)–(f) Conversion efficiency to synchrotron radiation for p-, s- and both left-hand and right-hand circular polarization, respectively.

a peak at  $\theta_i = 52.5^\circ$  that is only approximately  $0.5 \text{ J sr}^{-1}$  higher than the result for normal incidence, less than the factor of two improvement observed in 2D. The magnitude of the angle-resolved emission in each direction appears to converge around  $\theta_i = 60^\circ$ , before the magnitude of the  $\theta_{0,-90}$  lobe unexpectedly peaks again for  $\theta_i = 67.5^\circ$ ; such behaviour was not observed in the 2D simulations shown in Figure 8(a). The conversion efficiency for p-polarization is shown in Figure 9(d), where the overall synchrotron conversion efficiency peaks for  $\theta_i = 45^\circ$  while the conversion efficiency to  $\theta_{0,-90}$ -directed emission peaks at approximately twice its normal incidence value.

For an s- (along  $z$ ) polarized laser pulse, the synchrotron lobes are oriented perpendicular to those for p-polarization because they are generated along the axis of polarization of the laser light. Therefore, each lobe is defined by their polar angle,  $\phi$ . In Figure 9(b), the lobes begin at normal incidence with approximately equal magnitude and have similar values to those for p-polarization. However, for increasing  $\theta_i$  the magnitude of the emission in each polar direction tends to reduce. The overall conversion efficiency to synchrotron radiation also reduces in a similar way in Figure 9(e) and remains equal for each polar direction. Rotating the target causes the laser pulse to be spread over a larger area, and to be reflected obliquely. As a result, the radiation pressure that is required for forming a cavity in the target and producing strong laser-injected emission is lowered. Furthermore, because the laser pulse is polarized parallel with the target surface, its electric field cannot directly pull electrons away

from the surface and further into its spatial profile without deformation of the surface.

Finally, in Figures 9(c) and 9(f), results for both left-hand circular polarization (LHCP) and right-hand circular polarization (RHCP) are shown. For c-polarization, two lobes are not produced for normal incidence, but an annular structure instead<sup>[27]</sup>, due to the rotating electric field pulling electrons into the focal spot from all around the sides of the hole bored plasma cavity by the time it has completed one cycle. The magnitude of the angle-resolved energy of synchrotron emission in the full angular range is shown in Figure 9(c). For normal incidence it is approximately  $0.5 \text{ J sr}^{-1}$ , which is approximately  $1 \text{ J sr}^{-1}$  lower than for linear polarization. However, this more than doubles in rotating the target to  $\theta_i = 45^\circ$ . The magnitude of the emission reduces for  $\theta_i = 60^\circ$  before peaking again for  $67.5^\circ$  in a similar way to the p-polarization results. The conversion efficiency in Figure 9(f) remains approximately constant for  $\theta_i = 0^\circ$ – $45^\circ$ , before it quickly reduces for larger  $\theta_i$ . The results here for LHCP and RHCP are almost identical.

The results in Figure 9 indicate that p-polarization and  $\theta_i \approx 45^\circ$ – $52.5^\circ$  produce the optimal combination of peak angle-resolved energy of synchrotron emission and conversion efficiency for the target simulated. However, they do not capture all of the changes to the spatial structure of the synchrotron emission. In Figure 10 the angle-resolved synchrotron emission in the forward direction ( $|\theta| < 90^\circ$ ) is shown for each polarization and a number of different values of  $\theta_i$ .

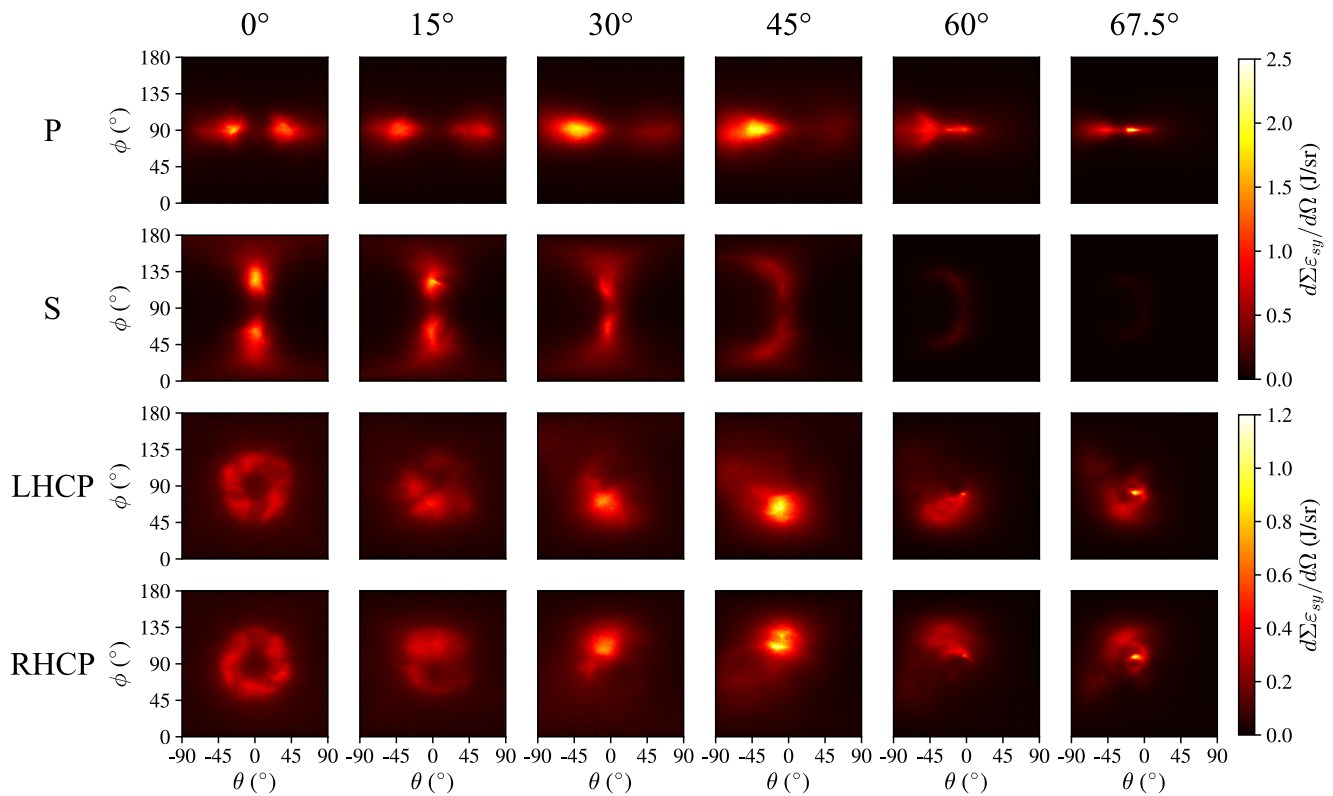


**Figure 10.** Angular profiles of the total energy of synchrotron emission in the forward direction ( $|\theta| < 90^\circ$ ) in 3D simulations for different laser light polarization states and angles-of-incidence.

For p-polarization a double lobe structure is shown for  $\theta = 0^\circ$ – $45^\circ$ , in which the  $\theta_{0,-90}$  lobe gains energy up to  $45^\circ$ , whilst the  $\theta_{90,0}$  lobe disappears. When  $\theta_i = 60^\circ$  the angular structure changes, a beam of synchrotron radiation narrow in  $\phi$  ( $|\phi - 90^\circ| < 5^\circ$ ) is produced for  $\theta = -25^\circ$ – $0^\circ$ , becoming wider like the original lobe structure for lower  $\theta$ , and the magnitude is strongly reduced. Lastly, for  $\theta_i = 67.5^\circ$ , the full synchrotron emission profile becomes narrower in  $\phi$  and strongest for  $\theta$  between  $-20^\circ$  and  $-10^\circ$ . This variation with  $\theta_i$  is not replicated for s-polarization, where only the double lobe structure is present and reduces in magnitude for increasing  $\theta_i$ , although it curves towards the  $-\theta$  direction.

For  $\theta_i = 67.5^\circ$  the angle between the laser propagation direction and target surface becomes  $22.5^\circ$ , approaching the divergence half-angle of the laser pulse,  $\theta_{\text{div}} = \sqrt{2 \ln 2} \lambda_L / \pi \phi_L = 17.2^\circ$ . When a component of the laser polarization is in the plane of target rotation, as is the case for p- and c-polarization, the laser electric field can inject electrons from close to the target surface further into the laser pulse as it focuses. The electrons are accelerated along the target surface, over a distance much greater than  $\phi_L$ , towards the focal point where they strongly emit synchrotron radiation in the intense fields. Because the accelerated electron bunches that reach the centre of the laser focus have a narrow divergence, the beam of synchrotron radiation also has a narrow divergence. For the larger  $\theta_i$  value

of  $75^\circ$ , this mechanism is degraded, as shown in [Figure 9\(a\)](#). The expansion of electrons from the target surface affects the laser beam propagation, and the reduced difference in the propagation direction of the laser pulse and electrons moving parallel with the surface will act to reduce  $\chi_e$  and the synchrotron emission.

For LHCP and RHCP in [Figure 10](#), synchrotron radiation is generated with an annular spatial profile for normal incidence. Rotation of the target, however, produces an asymmetry in the angular distribution of radiation. One section of the annular structure becomes thicker and brighter, the hole of the annulus moves away from  $\theta = 0^\circ$  and  $\phi = 90^\circ$  and the opposite side of the annulus becomes thinner and dimmer. The spatial profile of the synchrotron radiation now shows its dependence upon the direction of rotation of circular polarization, and the profile is flipped in  $\phi$  from LHCP to RHCP. For increasing target rotation, the annular structure disappears and a broad arc of synchrotron radiation is formed with a brighter spot in a single direction. Rotation of the target reduces the number of electrons on one side of the focal spot, thus reducing the number of electrons drawn into the spot by the laser electric field on this side. As the electric field rotates it pulls most electrons from the rotated ( $\theta_i > 0^\circ$ ) target into the focal spot after it points in the  $+y$  direction, which results in the production of angular distributions of electrons in the field that are either directed in the

$+z$  ( $\phi < 90^\circ$ ) or  $-z$  ( $\phi > 90^\circ$ ) directions, depending on the direction of rotation of the electric field. For LHCP, the electric field next rotates towards the  $-z$  direction, accelerating electrons in the  $+z$  direction and generating synchrotron radiation in the same direction as those electrons. The situation is reversed for RHCP, directing electrons in the field in the  $-z$  direction and the concomitant synchrotron radiation.

For  $\theta_i \geq 60^\circ$ , the narrow enhanced beam of synchrotron radiation obtained from the acceleration of electrons along the target surface with the edge of the focusing laser beam appears, similar to the changes to the angular synchrotron profile for p-polarization. However, due to the rotation of the electric field vector, the synchrotron radiation is emitted in a small angle above the  $xy$  plane for LHCP and below the  $xy$  plane for RHCP.

A limited number of 3D simulations were performed for  $I_L = 3 \times 10^{23} \text{ W cm}^{-2}$ , corresponding to a laser energy of 109 J, to identify if the spatial structures in the synchrotron emission change when the target is strongly deformed by the radiation pressure. The angle-resolved total energy of synchrotron emission for these simulations is shown in the [Supplementary Materials](#). An  $l = 1 \mu\text{m}$  and  $3 \mu\text{m}$  target was simulated due to the high laser transmission of the former target for normal incidence at this intensity. The values of  $\theta_i$  were limited to  $0^\circ$ ,  $45^\circ$  and  $67.5^\circ$ .

The strongest angle-resolved synchrotron emission of  $160 \text{ J sr}^{-1}$  was generated for p-polarization,  $\theta_i = 45^\circ$  and  $l = 3 \mu\text{m}$ . However, this corresponds to a narrow beam centred at  $\theta \approx 0^\circ$  and  $\phi \approx 90^\circ$ , instead of an oblique single lobe as in [Figure 10](#). The emission here is driven by electrons from the  $y > 0$  side of the target injected into the laser pulse and co-propagating with it as it moves further into the target. This is the same mechanism that drives similar emission for the optimum of  $f_{O2}$  in [Figure 7\(c\)](#), enabled here by the reduced density modelled in 3D. The double lobes for p- and s-polarization are generated closer to the laser propagation direction, and the synchrotron emission for s-polarization is less strongly suppressed for  $l = 3 \mu\text{m}$  with increasing  $\theta_i$  due to the increased target deformation. For c-polarization, the emission is also more collimated with the laser pulse, and the annular structure for normal incidence only appears for  $l = 1 \mu\text{m}$ , with the  $l = 3 \mu\text{m}$  target producing a spot centred close to the laser propagation direction. For all of these polarization states and  $l = 1 \mu\text{m}$ , the peak angle-resolved emission is enhanced for the larger values of  $\theta_i$  due to the increased target material within the path of the laser pulse.

## 8. Summary

In summary, Bayesian optimization has been applied to the generation of synchrotron radiation in ultrahigh-intensity laser interactions with CH foils in 2D simulations. Optimization of individual properties is shown, and control

of simultaneous optimization of the conflicting objectives of maximizing synchrotron production and minimizing bremsstrahlung emission is demonstrated with changes to the objective function, including the use of an acceptance function.

Through the use of machine learning-based optimization, the angle-of-incidence is identified as a critical parameter in achieving the greatest angle-resolved synchrotron emission. Further 2D and 3D simulations of a  $3 \times 10^{22} \text{ W cm}^{-2}$  intensity, 30 fs pulse duration,  $1 \mu\text{m}$  spot size and 10.9 J energy laser pulse support the optimization of the synchrotron emission spatial profile into a single forward-directed lobe. The polarization of the laser pulse is shown to control the angular distribution of synchrotron radiation, due to the synchrotron emission being dominated by electrons pulled into the laser pulse by the laser electric field. Changing the direction of rotation of the electric field vector for circular polarization is shown to flip the spatial profile of the synchrotron emission in the  $z$  (polar) direction. Furthermore, rotation of the target to bring the surface close to the divergence half-angle of the tightly focused laser pulse is observed to produce a narrow beam of synchrotron radiation from the electrons accelerated along the surface, provided the laser light is not s-polarized.

The changes induced in the synchrotron spatial profile with laser polarization and angle-of-incidence may enable such radiation to be more easily distinguishable from bremsstrahlung emission, and enhance studies of the QED-plasma physics in these interactions. The demonstrated control of the synchrotron emission is also useful for the application of this intense source of high-energy photons. The work presented here may be further extended by considering the generation of electron–positron pairs from the high-energy photons in the intense laser fields, and the influence of parameters not explored, such as the front surface density scale length, the spatial-intensity contrast<sup>[89]</sup> and different target structures.

## Acknowledgements

This work was financially supported by EPSRC (grant Nos. EP/R006202/1 and EP/V049232/1) and STFC (grant No. ST/V001612/1). The ARCHER2 high-performance computer was used, with access provided via the Plasma Physics HEC Consortia (EP/R029148/1). Additional work was performed using resources provided by the Cambridge Tier-2 system operated by the University of Cambridge Research Computing Service ([www.hpc.cam.ac.uk](http://www.hpc.cam.ac.uk)), funded by EPSRC Tier-2 capital grant EP/T022159/1. EPOCH was developed under EPSRC grant EP/G054940/1. The research also received funding from Laserlab-Europe (grant agreement No. 871124, European Union's Horizon 2020 research and innovation programme). Data associated with research published in this paper can be accessed at <http://doi.org/10.15129/d197dd97-721b-4afe-b241-218ece8af3e6>.

## Supplementary Materials

To view supplementary material for this article, please visit <http://doi.org/10.1017/hpl.2023.11>.

## References

- H. Schwoerer, P. Gibbon, S. Düsterer, R. Behrens, C. Ziener, C. Reich, and R. Sauerbrey, *Phys. Rev. Lett.* **86**, 2317 (2001).
- C. D. Chen, A. J. Kemp, F. Pérez, A. Link, F. N. Beg, S. Chawla, M. H. Key, H. McLean, A. Morace, Y. Ping, A. Sorokovikova, R. B. Stephens, M. Streeter, B. Westover, and P. K. Patel, *Phys. Plasmas* **20**, 052703 (2013).
- S. Singh, C. D. Armstrong, N. Kang, L. Ren, H. Liu, N. Hua, D. R. Rusby, O. Klimo, R. Versaci, Y. Zhang, M. Sun, B. Zhu, A. Lei, X. Ouyang, L. Lancia, A. L. Garcia, A. Wagner, T. Cowan, J. Zhu, T. Schlegel, S. Weber, P. McKenna, D. Neely, V. Tikhonchuk, and D. Kumar, *Plasma Phys. Control. Fusion* **63**, 035004 (2021).
- A. Rousse, P. Audebert, J. P. Geindre, F. Fallières, J. C. Gauthier, A. Mysyrowicz, G. Grillon, and A. Antonetti, *Phys. Rev. E* **50**, 2200 (1994).
- R. D. Edwards, M. A. Sinclair, T. J. Goldsack, K. Krushelnick, F. N. Beg, E. L. Clark, A. E. Dangor, Z. Najmudin, M. Tatarakis, B. Walton, M. Zepf, K. W. D. Ledingham, I. Spencer, P. A. Norreys, R. J. Clarke, R. Kodama, Y. Toyama, and M. Tampo, *Appl. Phys. Lett.* **80**, 2129 (2002).
- J. Galy, M. Maučec, D. J. Hamilton, R. Edwards, and J. Magill, *New J. Phys.* **9**, 23 (2007).
- C. Courtois, R. Edwards, A. C. La Fontaine, C. Aedy, M. Barbotin, S. Bazzoli, L. Biddle, D. Brebion, J. L. Bourgade, D. Drew, M. Fox, M. Gardner, J. Gazave, J. M. Lagrange, O. Landoas, L. Le Dain, E. Lefebvre, D. Mastrosimone, N. Pichoff, G. Pien, M. Ramsay, A. Simons, N. Sircombe, C. Stoeckl, and K. Thorp, *Phys. Plasmas* **18**, 023101 (2011).
- C. M. Brenner, S. R. Mirfayzi, D. R. Rusby, C. Armstrong, A. Alejo, L. A. Wilson, R. Clarke, H. Ahmed, N. M. H. Butler, D. Haddock, A. Higginson, A. McClymont, C. Murphy, M. Notley, P. Oliver, R. Allott, C. Hernandez-Gomez, S. Kar, P. McKenna, and D. Neely, *Plasma Phys. Control. Fusion* **58**, 014039 (2016).
- K. W. D. Ledingham, I. Spencer, T. McCanny, R. P. Singhal, M. I. K. Santala, E. Clark, I. Watts, F. N. Beg, M. Zepf, K. Krushelnick, M. Tatarakis, A. E. Dangor, P. A. Norreys, R. Allott, D. Neely, R. J. Clark, A. C. Machacek, J. S. Wark, A. J. Cresswell, D. C. W. Sanderson, and J. Magill, *Phys. Rev. Lett.* **84**, 899 (2000).
- E. P. Liang, S. C. Wilks, and M. Tabak, *Phys. Rev. Lett.* **81**, 4887 (1998).
- T. E. Cowan, M. D. Perry, M. H. Key, T. R. Ditmire, S. P. Hatchett, E. A. Henry, J. D. Moody, M. J. Moran, D. M. Pennington, T. W. Phillips, T. C. Sangster, J. A. Sefcik, M. S. Singh, R. A. Snavely, M. A. Stoyer, S. C. Wilks, P. E. Young, Y. Takahashi, B. Dong, W. Fountain, T. Parnell, J. Johnson, A. W. Hunt, and T. Kühl, *Laser Part. Beams* **17**, 773 (1999).
- B. Shen and J. Meyer-ter Vehn, *Phys. Rev. E* **65**, 016405 (2001).
- H. Chen, S. C. Wilks, D. D. Meyerhofer, J. Bonlie, C. D. Chen, S. N. Chen, C. Courtois, L. Elbertson, G. Gregori, W. Krueer, O. Landoas, J. Mithen, J. Myatt, C. D. Murphy, P. Nilson, D. Price, M. Schneider, R. Shepherd, C. Stoeckl, M. Tabak, R. Tommasini, and P. Beiersdorfer, *Phys. Rev. Lett.* **105**, 015003 (2010).
- B. Martinez, M. Lobet, R. Ducloux, E. d'Humières, and L. Gremillet, *Phys. Plasmas* **26**, 103109 (2019).
- J. W. Yoon, Y. G. Kim, I. W. Choi, J. H. Sung, H. W. Lee, S. K. Lee, and C. H. Nam, *Optica* **8**, 630 (2021).
- F. Sauter, *Z. Phys.* **69**, 742 (1931).
- J. Schwinger, *Phys. Rev.* **82**, 664 (1951).
- A. M. Fedotov, N. B. Narozhny, G. Mourou, and G. Korn, *Phys. Rev. Lett.* **105**, 080402 (2010).
- G. Breit and J. A. Wheeler, *Phys. Rev.* **46**, 1087 (1934).
- A. R. Bell and J. G. Kirk, *Phys. Rev. Lett.* **101**, 200403 (2008).
- C. P. Ridgers, C. S. Brady, R. Ducloux, J. G. Kirk, K. Bennett, T. D. Arber, A. P. L. Robinson, and A. R. Bell, *Phys. Rev. Lett.* **108**, 165006 (2012).
- J. M. Cole, K. T. Behm, E. Gerstmayr, T. G. Blackburn, J. C. Wood, C. D. Baird, M. J. Duff, C. Harvey, A. Ilderton, A. S. Joglekar, K. Krushelnick, S. Kuschel, M. Marklund, P. McKenna, C. D. Murphy, K. Poder, C. P. Ridgers, G. M. Samarin, G. Sarri, D. R. Symes, A. G. R. Thomas, J. Warwick, M. Zepf, Z. Najmudin, and S. P. D. Mangles, *Phys. Rev. X* **8**, 011020 (2018).
- K. Poder, M. Tamburini, G. Sarri, A. Di Piazza, S. Kuschel, C. D. Baird, K. Behm, S. Böhlen, J. M. Cole, D. J. Corvan, M. Duff, E. Gerstmayr, C. H. Keitel, K. Krushelnick, S. P. D. Mangles, P. McKenna, C. D. Murphy, Z. Najmudin, C. P. Ridgers, G. M. Samarin, D. R. Symes, A. G. R. Thomas, J. Warwick, and M. Zepf, *Phys. Rev. X* **8**, 031004 (2018).
- C. S. Brady, C. P. Ridgers, T. D. Arber, A. R. Bell, and J. G. Kirk, *Phys. Rev. Lett.* **109**, 245006 (2012).
- T. Nakamura, J. K. Koga, T. Zh. Esirkepov, M. Kando, G. Korn, and S. V. Bulanov, *Phys. Rev. Lett.* **108**, 195001 (2012).
- C. S. Brady, C. P. Ridgers, T. D. Arber, and A. R. Bell, *Phys. Plasmas* **21**, 033108 (2014).
- L. L. Ji, A. Pukhov, E. N. Nerush, I. Yu. Kostyukov, B. F. Shen, and K. U. Akli, *Phys. Plasmas* **21**, 023109 (2014).
- P. Hadjisolomou, T. M. Jeong, and S. V. Bulanov, *Sci. Rep.* **12**, 17143 (2022).
- P. Hadjisolomou, T. M. Jeong, P. Valenta, D. Kolenaty, R. Versaci, V. Olšovcová, C. P. Ridgers, and S. V. Bulanov, *J. Plasma Phys.* **88**, 905880104 (2022).
- P. Zhang, C. P. Ridgers, and A. G. R. Thomas, *New J. Phys.* **17**, 043051 (2015).
- D. A. Serebryakov and E. N. Nerush, *Quantum Electron.* **46**, 299 (2016).
- D. J. Stark, T. Toncian, and A. V. Arefiev, *Phys. Rev. Lett.* **116**, 185003 (2016).
- H. X. Chang, B. Qiao, T. W. Huang, Z. Xu, C. T. Zhou, Y. Q. Gu, X. Q. Yan, M. Zepf, and X. T. He, *Sci. Rep.* **7**, 45031 (2017).
- H.-Z. Li, T.-P. Yu, J.-J. Liu, Y. Yin, X.-L. Zhu, R. Capdessus, F. Pegoraro, Z.-M. Sheng, P. McKenna, and F.-Q. Shao, *Sci. Rep.* **7**, 17312 (2017).
- R. Capdessus, M. King, D. Del Sorbo, M. Duff, C. P. Ridgers, and P. McKenna, *Sci. Rep.* **8**, 9155 (2018).
- Z. Gong, R. H. Hu, H. Y. Lu, J. Q. Yu, D. H. Wang, E. G. Fu, C. E. Chen, X. T. He, and X. Q. Yan, *Plasma Phys. Control. Fusion* **60**, 044004 (2018).
- Y.-J. Gu, O. Klimo, S. V. Bulanov, and S. Weber, *Commun. Phys.* **1**, 93 (2018).
- O. Jansen, T. Wang, D. J. Stark, E. d'Humières, T. Toncian, and A. V. Arefiev, *Plasma Phys. Control. Fusion* **60**, 054006 (2018).
- K. V. Lezhnin, P. V. Sasorov, G. Korn, and S. V. Bulanov, *Phys. Plasmas* **25**, 123105 (2018).
- W. Luo, S.-D. Wu, W.-Y. Liu, Y.-Y. Ma, F.-Y. Li, T. Yuan, J.-Y. Yu, M. Chen, and Z.-M. Sheng, *Plasma Phys. Control. Fusion* **60**, 095006 (2018).
- B. Martinez, E. d'Humières, and L. Gremillet, *Plasma Phys. Control. Fusion* **60**, 074009 (2018).
- W.-M. Wang, Z.-M. Sheng, P. Gibbon, L.-M. Chen, Y.-T. Li, and J. Zhang, *Proc. Natl. Acad. Sci. U.S.A.* **115**, 9911 (2018).
- X.-L. Zhu, T.-P. Yu, M. Chen, S.-M. Weng, and Z.-M. Sheng, *New J. Phys.* **20**, 083013 (2018).

44. T. W. Huang, C. M. Kim, C. T. Zhou, M. H. Cho, K. Nakajima, C. M. Ryu, S. C. Ruan, and C. H. Nam, *New J. Phys.* **21**, 013008 (2019).
45. D. A. Serebryakov, T. M. Volkova, E. N. Nerush, and I. Y. Kostyukov, *Plasma Phys. Control. Fusion* **61**, 074007 (2019).
46. Y. Zhao, J. Liu, Y. Li, and G. Xia, *Plasma Phys. Control. Fusion* **61**, 065010 (2019).
47. T. Wang, X. Ribeyre, Z. Gong, O. Jansen, E. d'Humières, D. Stutman, T. Toncian, and A. Arefiev, *Phys. Rev. Appl.* **13**, 054024 (2020).
48. X.-B. Wang, G.-Y. Hu, Z.-M. Zhang, Y.-Q. Gu, B. Zhao, Y. Zuo, and J. Zheng, *High Power Laser Sci. Eng.* **8**, e34 (2020).
49. K. Xue, Z.-K. Dou, F. Wan, T.-P. Yu, W.-M. Wang, J.-R. Ren, Q. Zhao, Y.-T. Zhao, Z.-F. Xu, and J.-X. Li, *Matter Radiat. Extrem.* **5**, 054402 (2020).
50. Y. Zhao, J. Liu, G. Xia, and A. Bonatto, *Phys. Plasmas* **27**, 073106 (2020).
51. L. Fedeli, A. Sainte-Marie, N. Zaim, M. Thévenet, J. L. Vay, A. Myers, F. Quéré, and H. Vincenti, *Phys. Rev. Lett.* **127**, 114801 (2021).
52. P. Hadjisolomou, T. M. Jeong, P. Valenta, G. Korn, and S. V. Bulanov, *Phys. Rev. E* **104**, 015203 (2021).
53. Y. He, T. G. Blackburn, T. Toncian, and A. V. Arefiev, *Commun. Phys.* **4**, 139 (2021).
54. S. Chintalwad, S. Krishnamurthy, B. Ramakrishna, and C. P. Ridgers, *Phys. Rev. E* **105**, 025205 (2022).
55. F. Wan, C. Lv, M. Jia, H. Sang, and B. Xie, *Eur. Phys. J. D* **71**, 236 (2017).
56. J. Vyskočil, O. Klimo, and S. Weber, *Plasma Phys. Control. Fusion* **60**, 054013 (2018).
57. J. Vyskočil, E. Gelfer, and O. Klimo, *Plasma Phys. Control. Fusion* **62**, 064002 (2020).
58. S. Morris, A. Robinson, and C. Ridgers, *Phys. Plasmas* **28**, 103304 (2021).
59. B. Martinez, E. d'Humières, and L. Gremillet, *Phys. Rev. Res.* **2**, 043341 (2020).
60. V. A. Vshivkov, N. M. Naumova, F. Pegoraro, and S. V. Bulanov, *Phys. Plasmas* **5**, 2727 (1998).
61. S. Palaniyappan, B. M. Hegelich, H.-C. Wu, D. Jung, D. C. Gautier, L. Yin, B. J. Albright, R. P. Johnson, T. Shimada, S. Letzring, D. T. Offermann, J. Ren, C. Huang, R. Hörlein, B. Dromey, J. C. Fernandez, and R. C. Shah, *Nat. Phys.* **8**, 763 (2012).
62. C. S. Brady, C. P. Ridgers, T. D. Arber, and A. R. Bell, *Plasma Phys. Control. Fusion* **55**, 124016 (2013).
63. B. Shahriari, K. Swersky, Z. Wang, R. P. Adams, and N. de Freitas, *Proc. IEEE* **104**, 148 (2016).
64. P. I. Frazier, in *Recent Advances in Optimization and Modeling of Contemporary Problems* (INFORMS, 2018), p. 255.
65. S. Jalas, M. Kirchen, P. Messner, P. Winkler, L. Hübner, J. Dirkwinkel, M. Schnepf, R. Lehe, and A. R. Maier, *Phys. Rev. Lett.* **126**, 104801 (2021).
66. R. J. Shalloo, S. J. D. Dann, J.-N. Gruse, C. I. D. Underwood, A. F. Antoine, C. Arran, M. Backhouse, C. D. Baird, M. D. Balcazar, N. Bourgeois, J. A. Cardarelli, P. Hatfield, J. Kang, K. Krushelnick, S. P. D. Mangles, C. D. Murphy, N. Lu, J. Osterhoff, K. Pöder, P. P. Rajeev, C. P. Ridgers, S. Rozario, M. P. Selwood, A. J. Shahani, D. R. Symes, A. G. R. Thomas, C. Thornton, Z. Najmudin, and M. J. V. Streeter, *Nat. Commun.* **11**, 6355 (2020).
67. E. J. Dolier, M. King, R. Wilson, R. J. Gray, and P. McKenna, *New J. Phys.* **24**, 073025 (2022).
68. A. Gonoskov, E. Wallin, A. Polovinkin, and I. Meyerov, *Sci. Rep.* **9**, 7043 (2019).
69. B. Z. Djordjević, A. J. Kemp, J. Kim, R. A. Simpson, S. C. Wilks, T. Ma, and D. A. Mariscal, *Phys. Plasmas* **28**, 043105 (2021).
70. Z.-H. He, B. Hou, V. Lebailly, J. A. Nees, K. Krushelnick, and A. G. R. Thomas, *Nat. Commun.* **6**, 7156 (2015).
71. Z.-H. He, B. Hou, G. Gao, V. Lebailly, J. A. Nees, R. Clarke, K. Krushelnick, and A. G. R. Thomas, *Phys. Plasmas* **22**, 056704 (2015).
72. S. J. D. Dann, C. D. Baird, N. Bourgeois, O. Chekhlov, S. Eardley, C. D. Gregory, J.-N. Gruse, J. Hah, D. Hazra, S. J. Hawkes, C. J. Hooker, K. Krushelnick, S. P. D. Mangles, V. A. Marshall, C. D. Murphy, Z. Najmudin, J. A. Nees, J. Osterhoff, B. Parry, P. Pourmoussavi, S. V. Rahul, P. P. Rajeev, S. Rozario, J. D. E. Scott, R. A. Smith, E. Springate, Y. Tang, S. Tata, A. G. R. Thomas, C. Thornton, D. R. Symes, and M. J. V. Streeter, *Phys. Rev. Accel. Beams* **22**, 041303 (2019).
73. J. R. Smith, C. Orban, J. T. Morrison, K. M. George, G. K. Ngirang, E. A. Chowdhury, and W. M. Roquemore, *New J. Phys.* **22**, 103067 (2020).
74. K. Deb, in *Search Methodologies: Introductory Tutorials in Optimization and Decision Support Techniques* (Springer US, 2014), p. 403.
75. M. T. M. Emmerich and A. H. Deutz, *Nat. Comput.* **17**, 585 (2018).
76. R. Roussel, A. Hanuka, and A. Edelen, *Phys. Rev. Accel. Beams* **24**, 062801 (2021).
77. F. Irshad, S. Karsch, and A. Döpp, *Phys. Rev. Res.* **5**, 013063 (2023).
78. T. D. Arber, K. Bennett, C. S. Brady, A. Lawrence-Douglas, M. G. Ramsay, N. J. Sircombe, P. Gillies, R. G. Evans, H. Schmitz, A. R. Bell, and C. P. Ridgers, *Plasma Phys. Control. Fusion* **57**, 113001 (2015).
79. C. P. Ridgers, J. G. Kirk, R. Ducloux, T. G. Blackburn, C. S. Brady, K. Bennett, T. D. Arber, and A. R. Bell, *J. Comput. Phys.* **260**, 273 (2014).
80. D. Wu, X. T. He, W. Yu, and S. Fritzsche, *High Power Laser Sci. Eng.* **6**, e50 (2018).
81. F. Pedregosa, G. Varoquaux, A. Gramfort, V. Michel, B. Thirion, O. Grisel, M. Blondel, P. Prettenhofer, R. Weiss, V. Dubourg, J. Vanderplas, A. Passos, D. Cournapeau, M. Brucher, M. Perrot, and É. Duchesnay, *J. Mach. Learn. Res.* **12**, 2825 (2011).
82. M. Hoffman, E. Brochu, and N. de Freitas, in *UAI'11: Proceedings of the Twenty-Seventh Conference on Uncertainty in Artificial Intelligence* (AUAI Press, 2011), p. 327.
83. J. Goodman, M. King, R. Wilson, R. J. Gray, and P. McKenna, *New J. Phys.* **24**, 053016 (2022).
84. S. D. R. Williamson, R. J. Gray, M. King, R. Wilson, R. J. Dance, C. Armstrong, D. R. Rusby, C. Brabetz, F. Wagner, B. Zielbauer, V. Bagnoud, D. Neely, and P. McKenna, *New J. Phys.* **22**, 053044 (2020).
85. S. C. Wilks, W. L. Kruer, M. Tabak, and A. B. Langdon, *Phys. Rev. Lett.* **69**, 1383 (1992).
86. A. P. L. Robinson, P. Gibbon, M. Zepf, S. Kar, R. G. Evans, and C. Bellei, *Plasma Phys. Control. Fusion* **51**, 024004 (2009).
87. P. M. Nilson, J. R. Davies, W. Theobald, P. A. Jaanimagi, C. Mileham, R. K. Jungquist, C. Stoeckl, I. A. Begishev, A. A. Solodov, J. F. Myatt, J. D. Zuegel, T. C. Sangster, R. Betti, and D. D. Meyerhofer, *Phys. Rev. Lett.* **108**, 085002 (2012).
88. E. N. Nerush, I. Yu. Kostyukov, L. Ji, and A. Pukhov, *Phys. Plasmas* **21**, 013109 (2014).
89. R. Wilson, M. King, N. M. H. Butler, D. C. Carroll, T. P. Frazer, M. J. Duff, A. Higginson, R. J. Dance, J. Jarrett, Z. E. Davidson, C. D. Armstrong, H. Liu, S. J. Hawkes, R. J. Clarke, D. Neely, R. J. Gray, and P. McKenna, *Sci. Rep.* **12**, 1910 (2022).